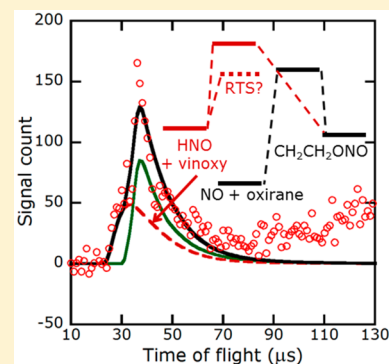


# Dissociation Pathways of the CH<sub>2</sub>CH<sub>2</sub>ONO Radical: NO<sub>2</sub> + Ethene, NO + Oxirane, and a Non-Intrinsic Reaction Coordinate HNO + Vinyoxy Pathway

Preston G. Scrape,<sup>†</sup> Trevor D. Roberts,<sup>†</sup> Shih-Huang Lee,<sup>‡</sup> and Laurie J. Butler<sup>\*,†</sup><sup>†</sup>The James Franck Institute and Department of Chemistry, The University of Chicago, Chicago, Illinois 60637, United States<sup>‡</sup>National Synchrotron Radiation Research Center, Hsinchu 30076, Taiwan, Republic of China

## Supporting Information

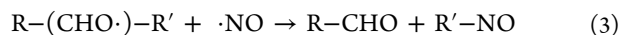
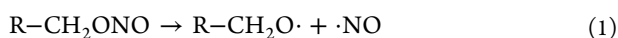
**ABSTRACT:** We first characterize the dissociation pathways of BrCH<sub>2</sub>CH<sub>2</sub>ONO, a substituted alkyl nitrite, upon photoexcitation at 193 nm under collision-free conditions, in a crossed laser–molecular beam scattering apparatus using vacuum ultraviolet photoionization detection. Three primary photodissociation pathways occur: photoelimination of HNO, leading to the products HNO + BrCH<sub>2</sub>CHO; C–Br bond photofission, leading to Br + CH<sub>2</sub>CH<sub>2</sub>ONO; and O–NO bond photofission, leading to NO + BrCH<sub>2</sub>CH<sub>2</sub>O. The data show that alkyl nitrites can eliminate HNO via a unimolecular mechanism in addition to the commonly accepted bulk disproportionation mechanism. Some of the products from the primary photodissociation pathways are highly vibrationally excited, so we then probe the product branching from the unimolecular dissociation of these unstable intermediates. Notably, the vibrationally excited CH<sub>2</sub>CH<sub>2</sub>ONO radicals undergo two channels predicted by statistical transition-state theory, and an additional non-intrinsic reaction coordinate channel, HNO elimination. CH<sub>2</sub>CH<sub>2</sub>ONO is formed with high rotational energy; by employing rotational models based on conservation of angular momentum, we predict, and verify experimentally, the kinetic energies of stable CH<sub>2</sub>CH<sub>2</sub>ONO radicals and the angular distribution of dissociation products. The major dissociation pathway of CH<sub>2</sub>CH<sub>2</sub>ONO is NO<sub>2</sub> + ethene, and some of the NO<sub>2</sub> is formed with sufficient internal energy to undergo further photodissociation. Nascent BrCH<sub>2</sub>CHO and CH<sub>2</sub>Br are also photodissociated upon absorption of a second 193 nm photon; we derive the kinetic energy release of these dissociations based on our data, noting similarities to the analogous photodissociation of ClCH<sub>2</sub>CHO and CH<sub>2</sub>Cl.



## 1. INTRODUCTION

Gaseous alkyl nitrites (R–ONO, where R is an alkyl group) are important intermediates in the formation of chemical smog and in the regulation of ozone levels.<sup>1–3</sup> Both photolysis and thermal decomposition of these species are rapid; photolysis under ultraviolet light occurs readily via photoabsorption in the nitrite moiety, which has absorption bands near 350 and 200 nm. The atmospheric impact of alkyl nitrite chemistry and photochemistry has motivated studies on nitrous acid (HONO),<sup>4–7</sup> methyl nitrite (CH<sub>3</sub>ONO),<sup>8–15</sup> and a number of higher nitrites as well.<sup>16–24</sup>

A common reaction pathway is dissociation to an alkoxy radical and nitric oxide, RONO → RO + NO.<sup>2,3</sup> In studies of the bulk kinetics of alkyl nitrites, nitrosoalkyl products (R–NO) are also observed, and the primary and secondary nitrites moreover evolve HNO + aldehyde or ketone.<sup>19–21</sup> A disproportionation mechanism for these pathways has been proposed in which nascent NO radicals recombine with nascent alkoxy radicals, leading either to H atom abstraction or C–C bond cleavage:<sup>3,22,23</sup>



There is also recent evidence of a unimolecular mechanism for HNO elimination. Zhu et al. have reported a roaming-mediated transition state for this process in methyl nitrite,<sup>13</sup> and Liu et al. did likewise for ethyl nitrite.<sup>25</sup> Homayoon and Bowman calculated a global potential energy surface for nitromethane and conducted a quasiclassical trajectory study on this surface;<sup>14,15</sup> they observed roaming trajectories leading to HNO from methyl nitrite (an isomer of nitromethane), mediated by the existence of a loosely bound van der Waals complex. Experimentally, Prozument et al. studied the pyrolysis of ethyl nitrite, concluding based on their data and a reaction mechanism model that the molecule evolves HNO by a

**Special Issue:** Piergiorgio Casavecchia and Antonio Lagana Festschrift

**Received:** December 28, 2015

**Revised:** March 7, 2016

unimolecular roaming mechanism.<sup>24</sup> One of the goals of the present study was to probe HNO production under collision-free conditions in photoexcited and vibrationally excited substituted nitrites.

Substituted alkyl nitrites, in which one or more H are replaced by another functional group such as a halogen (F, Cl, Br), pseudohalogen (OH), or radical center, are an interesting special case that has received less attention. The photochemistry of haloalkyl nitrites may differ from that of alkyl nitrites, for instance, because of competition between absorption in the halogen and nitrite chromophores. The prevalence of halocarbons and atomic halogens in arctic and marine atmospheres<sup>26,27</sup> suggests that haloalkoxy and haloalkyl nitrite chemistry may be significant in those regions. There is also recent evidence of significant inland sources of Cl.<sup>28</sup> Hydroxyalkoxy radicals (HO–R–O), related to hydroxyalkyl nitrites by the mechanisms described previously, appear in the atmospheric oxidation of alkenes.<sup>29</sup> Radicals of alkyl nitrites are formed by addition of NO<sub>2</sub> to a C=C double bond,<sup>30</sup> and they evince an unexpected absorption band at visible wavelengths that is not present in the closed-shell nitrites.<sup>18,30</sup>

The work reported here explores the photodissociation at 193 nm of 2-bromoethyl nitrite, BrCH<sub>2</sub>CH<sub>2</sub>ONO, under collision-free conditions, as a prototypical substituted alkyl nitrite. The photodissociation also produces the radical CH<sub>2</sub>CH<sub>2</sub>ONO (2-nitrosooxy ethyl), allowing us to probe the unimolecular dissociation of that species as well. This is an extension and conclusion of three previous studies of BrCH<sub>2</sub>CH<sub>2</sub>ONO by Chhantyal-Pun et al.<sup>31</sup> and Wang et al.<sup>32</sup> at 351/355 nm and Wang et al. at 193 nm.<sup>33</sup> Photodissociation of this molecule at 351/355 nm was found to proceed through O–NO bond fission, leading to the products NO + BrCH<sub>2</sub>CH<sub>2</sub>O.<sup>31,32</sup> No competition from either C–Br photofission or HBr photoelimination was observed; unimolecular dissociation to HNO was not considered. Photodissociation at 193 nm was found to proceed through both O–NO and C–Br bond fission, with a branching ratio between the two channels on the order of 4:1.<sup>33</sup> That study characterized the O–NO and C–Br primary photodissociation channels, as well as the secondary dissociation of vibrationally excited BrCH<sub>2</sub>CH<sub>2</sub>O following O–NO bond photofission, by 200 eV electron ionization detection of photoproducts. Moreover, the angular momentum of the CH<sub>2</sub>CH<sub>2</sub>ONO product following C–Br bond photofission was predicted by conservation of angular momentum using the measured Br photofragment velocity.

Herein, we present evidence of photoelimination of the BrCH<sub>2</sub>CH<sub>2</sub>ONO precursor, leading to HNO + BrCH<sub>2</sub>CHO, and dissociation of the vibrationally excited CH<sub>2</sub>CH<sub>2</sub>ONO radical (formed in C–Br photofission) to HNO + vinoxy. We also complement the previous study at 193 nm by characterizing all the secondary dissociation channels of CH<sub>2</sub>CH<sub>2</sub>ONO using tunable vacuum ultraviolet (VUV) photoionization detection. These results are presented in Sections 3.2 and 3.3. It was also necessary to analyze several other dissociation channels of the precursor and products, including multiphoton dissociations; we report the most interesting of these results in Sections 3.4 and 3.5 and provide the remainder of the data and analysis in the Supporting Information. Moreover, we slightly refine a few of the conclusions of the previous work in light of the new results of this study.

## 2. METHODS

**2.1. Preparation of 2-Bromoethyl Nitrite (BrCH<sub>2</sub>CH<sub>2</sub>ONO).** The photolytic precursor, BrCH<sub>2</sub>CH<sub>2</sub>ONO, was synthesized by the usual method of mixing the corresponding alcohol with sulfuric acid and sodium nitrite. We followed the same procedure as was used in the previous studies.<sup>31–33</sup> In short, 100 mL of aqueous NaNO<sub>2</sub> (4 M concentration) was cooled to 0 °C in an ice bath; to this solution was added a mixture of 0.4 mol BrCH<sub>2</sub>CH<sub>2</sub>OH, 0.2 mol concentrated H<sub>2</sub>SO<sub>4</sub>, and 7 mL of H<sub>2</sub>O, dropwise over 20 min with constant stirring. The organic layer of the product, containing BrCH<sub>2</sub>CH<sub>2</sub>ONO, was collected by separation from the aqueous layer; no further purification was performed. The product was stored in dry ice and used within one week.

**2.2. Crossed Laser–Molecular Beam Scattering Apparatus.** All data were collected at the National Synchrotron Radiation Research Center (NSRRC) in Hsinchu, Taiwan, using the U9 Chemical Dynamics Beamline and a crossed laser–molecular beam scattering apparatus. This apparatus has been described in detail elsewhere.<sup>34–36</sup> A molecular beam of BrCH<sub>2</sub>CH<sub>2</sub>ONO was created by first seeding the pure liquid, held at –10 °C, to its equilibrium vapor pressure in neon. The total backing pressure was ~600 Torr. The gas mixture was supersonically expanded into a rotating source chamber through a pulsed nozzle operating at 100 Hz, which was held at 60 °C to inhibit the formation of nitrite clusters. The rotating source was set at an angle of 15° with respect to the axis of the detector for all photodissociation experiments. The resulting molecular beam was then crossed perpendicularly with the unpolarized 193 nm output of a LPF 200 Lambda Physik Laser Technik laser, timed to fire ~240 μs after the nozzle so as to intersect the most dense region of the molecular beam pulse. The laser beam was focused to an area of ~12 mm<sup>2</sup> at its intersection with the molecular beam, and the pulse energy was maintained near 40 mJ.

After photodissociation, those fragments with net velocity vectors (the vector sum of the precursor molecule's velocity and the velocity imparted to recoiling fragments of photodissociation and secondary dissociation) pointing along the axis of the detector traveled 10.05 cm to enter the detector's ionizer, where they were photoionized by tunable VUV radiation from the synchrotron. This synchrotron output was first passed through a 30 cm gas cell containing ~10 Torr of argon to filter out higher harmonics. Ionized fragments were then propelled by a series of ion lenses through a quadrupole mass filter, and finally the mass-filtered ions were counted in a Daly detector. The time-dependent ion signal was binned by a multichannel scaler in 1 μs intervals measured from the time of the 193 nm laser shot, so this signal included both the neutral and ion flight times. The neutral flight time is recovered from the total by subtracting the ion's flight time, which is calculated using the calibrated ion flight constant of 5.43 μs amu<sup>-1/2</sup>; all of the time-of-flight (TOF) spectra in this report show only the neutral flight time.

Recoil kinetic energy distributions ( $P(E_T)$ s) for all dissociation events were fitted to the TOF spectra by forward convolution fitting using the CMLAB2 program.<sup>37</sup> The molecular beam velocity, which contributes to the fragments' net velocity vectors, was characterized using the photodepletion (hole-burning) method: the rotating source chamber was set on-axis with the detector, and the laser was operated at 50 Hz instead of 100 Hz, so that only one-half of all molecular beam

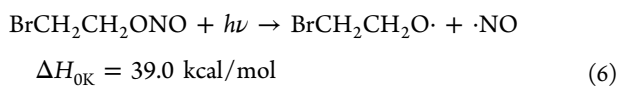
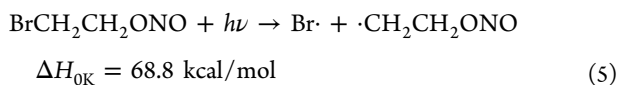
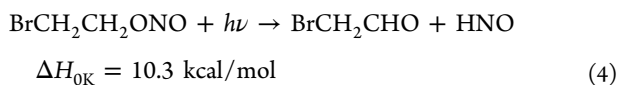
pulses underwent photodissociation. Subtraction of the “laser-on” ion signal from the “laser-off” ion signal gives the TOF distribution of the part of the molecular beam that photodissociates, which is easily transformed to a velocity distribution. Typical beam speeds were on the order of 700 m/s.

**2.3. Computational Methods.** All geometries and energies were calculated at the G4//B3LYP/6-311++G(3df,2p) level of theory using the Gaussian 09 software package.<sup>38</sup> All energies are zero-point corrected, and only the ground electronic state of each species is considered. Molecular geometries were rendered in the MOLDEN program.<sup>39</sup> To predict the rotational and vibrational energy imparted to nascent CH<sub>2</sub>CH<sub>2</sub>ONO radicals, and to obtain a first guess for the angular distribution of secondary dissociations from this radical, we used a model, described in detail elsewhere,<sup>40–42</sup> based on conservation of angular momentum and the observed C–Br primary photofission  $P(E_T)$ .

### 3. RESULTS

**3.1. Overview.** In the following subsections we present TOF data, derived recoil kinetic energy distributions, and angular distributions for fragments arising from primary and secondary dissociation events. By “primary photodissociation” we refer to the dissociation of the BrCH<sub>2</sub>CH<sub>2</sub>ONO precursor to two products upon absorption of a 193 nm photon; subsequent unimolecular dissociation of the nascent vibrationally excited photoproducts are termed “secondary dissociation”. The key results of this study are found in Section 3.2, in which we characterize the primary photodissociation channels including HNO photoelimination, and in Section 3.3, in which we examine the title system. For completeness, Sections 3.4 and 3.5 describe dissociation channels of the primary BrCH<sub>2</sub>CHO and BrCH<sub>2</sub>CH<sub>2</sub>O photofragments, including multiphoton effects; these channels contribute to the signal at  $m/e = 79$  (Br<sup>+</sup>) and  $m/e = 43$  (vinoxy cation). Additional data and analysis that may be of interest to some readers are supplied in the Supporting Information.

Our results indicate that three primary photodissociation pathways occur upon irradiation at 193 nm:



As was noted by Wang et al.,<sup>33</sup> BrCH<sub>2</sub>CH<sub>2</sub>ONO has multiple conformers: the C–Br bond may be anti or gauche with respect to the C–O bond, and the terminal N=O bond may be cis or trans with respect to the C–C bond. Analogously, each of BrCH<sub>2</sub>CH<sub>2</sub>O, BrCH<sub>2</sub>CHO, and CH<sub>2</sub>CH<sub>2</sub>ONO has multiple conformers. The (zero-point corrected) enthalpies of the reactions shown in eqs 4, 5, and 6 were calculated using the lowest-energy conformer of each species. The barriers to interconversion are low, on the order of a few kilocalories per mole, so we expect nontrivial populations of each possible conformer in these experiments. Our results should therefore

be considered a weighted average of the photochemistry of the individual conformers.

The products of primary photodissociation are formed with a range of internal energies. In our discussions of secondary dissociation, we compare the internal energy of a product to the energetic barriers along its potential energy surface to assess which dissociation pathways are energetically favorable. The internal energy distribution,  $E_{\text{int}}(\text{R})$ , of a radical R arising from photodissociation of a precursor R–X (herein, BrCH<sub>2</sub>CH<sub>2</sub>ONO) is calculated by conservation of energy:

$$E_{\text{int}}(\text{R-X}) + h\nu = \Delta H_{0\text{K}} + E_T + E_{\text{int}}(\text{R}) + E_{\text{int}}(\text{X}) \quad (7)$$

where  $E_{\text{int}}(\text{R-X})$  is the internal energy of the precursor,  $h\nu$  is the photon energy,  $E_T$  is the recoil kinetic energy imparted to the photoproducts, and  $E_{\text{int}}(\text{R})$  and  $E_{\text{int}}(\text{X})$  are the internal energies of the departing fragments R and X. In these experiments, supersonic expansion of the precursor cools molecular rotations, so  $E_{\text{int}}(\text{BrCH}_2\text{CH}_2\text{ONO})$  is simply the thermal vibrational energy at the nozzle temperature of 60 °C, which we calculate as 3 kcal/mol. The energy of a 193 nm photon is  $h\nu = 147.8$  kcal/mol. For a primary photodissociation process, the value of  $\Delta H_{0\text{K}}$  is one of those given in eqs 4, 5, or 6. Each recoil kinetic energy distribution,  $P(E_T)$ , was derived by forward convolution fitting: the  $P(E_T)$ s for all dissociations were iteratively adjusted to make the forward-convolution prediction of neutral flight times well-fitted to the experimentally observed neutral flight times at all masses.  $E_{\text{int}}(\text{X})$  is the internal energy of the cofragment X of species R; this term is discussed for X = Br, NO, and HNO in the relevant sections below.

In much of the data, there is a broad signal beginning at a neutral flight time of ~100 μs, rising to a peak near 220 μs. The signal does not depend on the 193 nm laser pulse, so it is assuredly not from any photodissociation event, including photodissociation of clusters; we therefore attribute it to time-dependent background from the scattered molecular beam pulse. (The data in this study show no observable contribution from photodissociation of clusters, because the appearance energy of daughter ions from photoionization of BrCH<sub>2</sub>CH<sub>2</sub>ONO is higher than the photon energy used. Wang et al. in their prior study at 193 nm using 200 eV electron bombardment ionization, observed a significant amount of signal from that source.) This signal causes no complications for the analysis of most fragments, as it is typically either too far from the photofragment peaks to overlap them or else is insignificantly small. In three cases (namely, at  $m/e = 29$ , 30, and 44), it was helpful to collect background data with the laser off and subtract that background from the “laser-on” data to eliminate the background that overlapped the product signals. In all of the figures below, we show the data with no background subtraction; the “laser-off” signal and background-subtracted data are provided in the Supporting Information.

**3.2. Primary Photodissociation Channels of BrCH<sub>2</sub>CH<sub>2</sub>ONO.** **3.2.1. Primary Photodissociation Leading to Br + CH<sub>2</sub>CH<sub>2</sub>ONO.** Primary C–Br photofission was characterized by the TOF data at  $m/e = 79$  (Br<sup>+</sup>) shown in Figure 1, collected at a synchrotron energy of 15.34 eV. The forward convolution fit corresponding to primary Br is depicted as a solid brown line peaking near 55 μs; the  $P(E_T)$  for this fit is given in Figure 2 as a brown line, which extends from ~15 kcal/mol to ~45 kcal/mol, with a maximum near 30 kcal/mol. (This experiment could not distinguish the spin–orbit states of Br

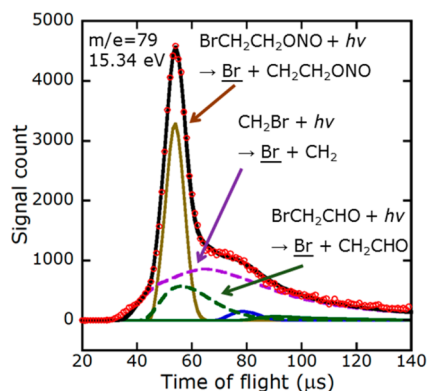


**Figure 1.** TOF spectrum of the signal at  $m/e = 79$  ( $\text{Br}^+$ ) with a photon energy of 15.34 eV. The sharp signal arises from primary photodissociation of  $\text{BrCH}_2\text{CH}_2\text{ONO}$  to  $\text{Br} + \text{CH}_2\text{CH}_2\text{ONO}$ , fit by a solid brown line peaking at  $\sim 55$   $\mu\text{s}$ . The other two labeled contributions are photodissociation of the  $\text{CH}_2\text{Br}$  product of secondary dissociation of  $\text{BrCH}_2\text{CH}_2\text{O}$  (dashed purple line, Section 3.5.2); and photodissociation of the  $\text{BrCH}_2\text{CHO}$  formed by photoelimination of  $\text{HNO}$  from  $\text{BrCH}_2\text{CH}_2\text{ONO}$  (dashed green line, Section 3.4.1). The two minor, unlabeled contributions are dissociative ionization of  $\text{BrCH}_2\text{CHO}$  from secondary dissociation of  $\text{BrCH}_2\text{CH}_2\text{O}$  (solid blue line peaking near 80  $\mu\text{s}$ , Section 3.5.3) and from photoelimination of  $\text{HNO}$  from  $\text{BrCH}_2\text{CH}_2\text{ONO}$  (solid green line with a maximum near 90  $\mu\text{s}$ , Section 3.2.2).

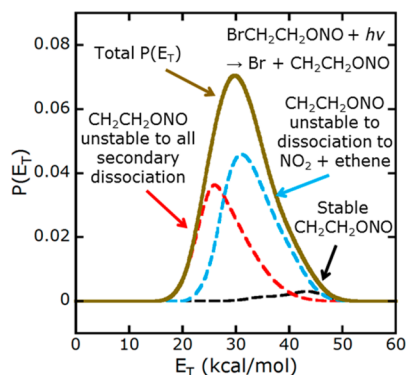


**Figure 2.** Photofragment recoil kinetic energy distribution,  $P(E_T)$ , of the  $\text{Br}$  and  $\text{CH}_2\text{CH}_2\text{ONO}$  cofragments resulting from  $\text{C-Br}$  bond photofission in  $\text{BrCH}_2\text{CH}_2\text{ONO}$ . The total  $P(E_T)$  (solid brown line), peaking near 30 kcal/mol, is derived by forward convolution fitting of the signal at  $m/e = 79$  ( $\text{Br}^+$ ), shown in Figure 1; the total  $P(E_T)$  gives the fit of the solid brown line in that figure. The total  $P(E_T)$  is partitioned into three components, corresponding to the amount of vibrational energy that the  $\text{CH}_2\text{CH}_2\text{ONO}$  fragment is expected to acquire at each  $E_T$ . See the text for details.

nor the conformers of  $\text{BrCH}_2\text{CH}_2\text{ONO}$ . For this reason, the  $P(E_T)$  should be considered an ensemble average.) Other contributions to the signal are dissociative ionization of primary  $\text{BrCH}_2\text{CHO}$  (Section 3.2.2), fitted as a solid green line; dissociative ionization of  $\text{BrCH}_2\text{CHO}$  formed by dissociation of  $\text{BrCH}_2\text{CH}_2\text{O}$ , discussed in the Supporting Information and fitted as a solid blue line; photodissociation of the secondary  $\text{CH}_2\text{Br}$  fragment from primary  $\text{BrCH}_2\text{CH}_2\text{O}$ , discussed in Section 3.5.2 and fitted as a dashed purple line; and secondary photodissociation of primary  $\text{BrCH}_2\text{CHO}$ , the cofragment of  $\text{HNO}$ , discussed in Section 3.4.1 and fitted as a dashed blue line.

Primary  $\text{C-Br}$  photodissociation was first observed in the previous study at 193 nm by Wang et al.<sup>33</sup> The distribution of recoil kinetic energy,  $P(E_T)$ , imparted to the  $\text{C-Br}$  photofission products reported by Wang et al. differs slightly from that in Figure 2: theirs is overall slower by a few kilocalories per mole, extending from  $\sim 10$  to  $\sim 40$  kcal/mol, with a maximum just under 30 kcal/mol. This disagreement is explained in Section 3.5.1; briefly, it is an artifact of the large signal due to nitrite clusters in the previous experiment, which interfered with analysis of the data at  $m/e = 93$  ( $\text{CH}_2\text{Br}^+$ ).

The  $\text{CH}_2\text{CH}_2\text{ONO}$  radical cofragment from  $\text{C-Br}$  photofission is formed with a range of internal energies determined by conservation of energy; key stationary points along its potential energy surface are plotted in Figure 3. The lowest barrier to dissociation is a transition state 11.1 kcal/mol higher in energy than the *trans* conformer, which leads to the products  $\text{NO}_2 + \text{ethene}$ . Given the  $P(E_T)$  of Figure 2, assuming that all of the  $\text{Br}$  is formed in its ground  $^2\text{P}_{3/2}$  spin-orbit state, and letting  $\Delta H_{0\text{K}} = 68.8$  kcal/mol (the endoergicity of transformation from the lowest-energy conformer of  $\text{BrCH}_2\text{CH}_2\text{ONO}$  to the lowest-energy conformer of the radical), the radicals are formed with an internal energy ranging from 38 to 68 kcal/mol (see the conservation-of-energy equation, eq 7). As was noted in the previous study, a significant fraction of this  $E_{\text{int}}$  is partitioned into rotation. To estimate the amount of vibrational energy in these fragments, we use a model based on conservation of angular momentum, described previously.<sup>40–42</sup> Briefly, this model assumes that the dissociating molecule behaves essentially classically, with the departing  $\text{Br}$  applying an instantaneous impulse along the  $\text{C-Br}$  bond, which produces the measured kinetic energy release of the dissociation. The angular momentum of the  $\text{CH}_2\text{CH}_2\text{ONO}$  “moiety” is readily calculated from the measured velocity imparted to the  $\text{Br}$  atom from the impulsive force (because linear and total angular momentum is conserved) and mapped onto the minimum-energy geometry of the  $\text{CH}_2\text{CH}_2\text{ONO}$  radical. The rotational energy  $E_{\text{rot}}$  of the radical is calculated from its angular momentum, and then its vibrational energy is simply  $E_{\text{vib}} = E_{\text{int}} - E_{\text{rot}}$ . The model then accounts for thermal vibrational energy in the precursor by repeating this calculation at several geometries along a normal vibrational mode of  $\text{BrCH}_2\text{CH}_2\text{ONO}$ . Because of thermal vibration, each  $E_T$  leads to many values of  $E_{\text{vib}}$ , the latter depending on the molecular geometry at the moment of impulse.

We require additional assumptions to apply this model to  $\text{BrCH}_2\text{CH}_2\text{ONO}$ . First, since both the precursor and the radical have *trans*- $\text{ONO}$  and *cis*- $\text{ONO}$  conformers, we assume that both of the *trans* conformers of the precursor photodissociate to the *trans* conformer of the radical, and likewise for the *cis* configuration (noting that, in both the precursor and the radical, the terminal  $\text{NO}$  may lie in or out of the plane of the  $\text{CCO}$  atoms). This association seems eminently reasonable, as alkyl bromides excited at 193 nm access a repulsive excited state, so the  $\text{ONO}$  moiety might be expected not to isomerize on the time scale of the dissociation. Second, we assume that the six conformers of the precursor are thermally populated at the nozzle temperature. Third, since this experiment is unable to determine the branching ratio between the two spin-orbit states of bromine (which differ in energy by 10.5 kcal/mol), we derive the vibrational energy distribution for  $\text{CH}_2\text{CH}_2\text{ONO}$  radicals assuming they are formed in coincidence with  $\text{Br}(^2\text{P}_{3/2})$ . This assumption leads us to predict a higher average  $E_{\text{vib}}$  than if  $\text{Br}(^2\text{P}_{1/2})$  were also considered.

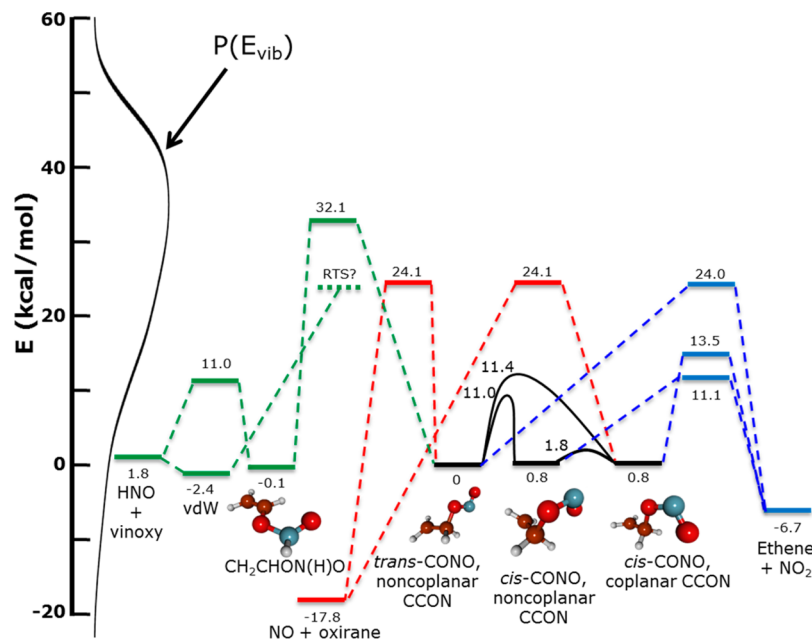


**Figure 3.** Stationary points along the potential energy surface of  $\text{CH}_2\text{CH}_2\text{ONO}$ , calculated using the G4//B3LYP/6-311++G(3df,2p) method. Energies are zero-point corrected and are given relative to the trans conformer. We have not found a transition state leading to the HNO + vinyoxy van der Waals well, but we estimate that the energetic barrier (labeled RTS?) to this roaming or non-IRC channel is best approximated by the barrier to NO + oxirane. The calculation of the vibrational energy distribution of the trans conformer of the radical,  $P(E_{\text{vib}})$ , is described in the text.

The predictions of our model for the partitioning of  $E_{\text{int}}$  between rotation and vibration are included in Figure 2 and Figure 3. Overlaid on Figure 3 is the predicted  $P(E_{\text{vib}})$ , a statistical average of the  $P(E_{\text{vib}})$  for dissociation from each of the precursor conformers. The model allowed us to divide the  $P(E_{\text{T}})$  of Figure 2 into three components. The red dashed line peaking near 25 kcal/mol represents the portion of the  $P(E_{\text{T}})$  leading to  $\text{CH}_2\text{CH}_2\text{ONO}$  radicals with  $E_{\text{vib}}$  above the dissociation barrier to NO + oxirane. The blue dashed line peaking near 30 kcal/mol is the portion leading to radicals with  $E_{\text{vib}}$  below the barrier to NO + oxirane but above the lowest-energy barrier to  $\text{NO}_2$  + ethene. The bimodal black dashed line is the portion leading to radicals with  $E_{\text{vib}}$  below the lowest-energy barrier to  $\text{NO}_2$  + ethene; these latter radicals are stable to all secondary dissociations, so they can enter the ionizer and be dissociatively ionized. Dissociative ionization of stable  $\text{CH}_2\text{CH}_2\text{ONO}$  is observed as  $\text{NO}^+$  at  $m/e = 30$ , discussed in Section 3.2.3. Secondary unimolecular dissociation of the radicals formed with higher vibrational energies is discussed in Section 3.3.

**3.2.2. Primary Photoelimination Leading to HNO + BrCH<sub>2</sub>CHO.** Figure 4 shows the TOF data for  $m/e = 31$ , representing fragments that ionize to  $\text{HNO}^+$ , taken with a synchrotron energy of 12.07 eV. We fitted the data by a sum of two contributions: primary photodissociation of  $\text{BrCH}_2\text{CH}_2\text{ONO}$  to HNO + BrCH<sub>2</sub>CHO (2-bromoacetaldehyde), with the HNO photoproduct signal fit in a green line with a peak near 40  $\mu\text{s}$ , and secondary dissociation of  $\text{CH}_2\text{CH}_2\text{ONO}$  radicals to HNO + CH<sub>2</sub>CHO (vinyoxy), with the fit to the HNO products shown in dashed red line with a peak near 30  $\mu\text{s}$ . The latter channel is discussed in Section 3.3.3. The sum of the two gives the total fit, shown as a black line. (The rising signal at long times, which is not from photofragments, is discussed in Section 3.1.) Figure 5 shows the recoil kinetic energy distribution,  $P(E_{\text{T}})$ , for the  $\text{BrCH}_2\text{CH}_2\text{ONO} \rightarrow \text{HNO} + \text{BrCH}_2\text{CHO}$  photofragmentation

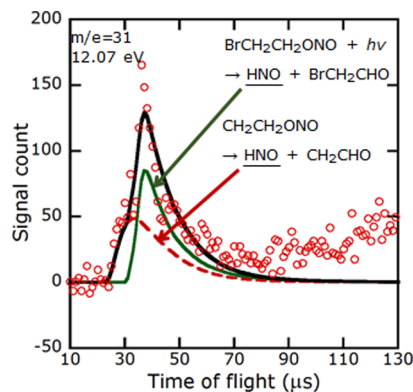


**Figure 4.** TOF spectrum of the signal at  $m/e = 31$  ( $\text{HNO}^+$ ) with a synchrotron energy of 12.07 eV. Primary photodissociation of  $\text{BrCH}_2\text{CH}_2\text{ONO}$  to  $\text{BrCH}_2\text{CHO} + \text{HNO}$  is fit by the solid green line, peaking near 40  $\mu\text{s}$ . Secondary dissociation of  $\text{CH}_2\text{CH}_2\text{ONO}$  radicals to  $\text{CH}_2\text{CHO}$  (vinyoxy) + HNO is fit by the dashed red line, peaking near 30  $\mu\text{s}$ .

channel, derived by fitting the contribution to the signal shown in green line to Figure 4. The  $P(E_{\text{T}})$  is broad, with a maximum at  $\sim 20$  kcal/mol. The velocity distribution of the momentum-matched  $\text{BrCH}_2\text{CHO}$  cofragment is also accurately fitted by this  $P(E_{\text{T}})$ , manifesting as dissociative ionization of  $\text{BrCH}_2\text{CHO}$  to  $\text{CH}_3^+$  (data in Section 3.4.2) and  $\text{CHO}^+$  (data in the Supporting Information); thus, the derived  $P(E_{\text{T}})$  is verified.

This photodissociation produces HNO and  $\text{BrCH}_2\text{CHO}$  with a large amount of internal energy, which can lead to secondary dissociation. Using the  $P(E_{\text{T}})$  of Figure 5 and  $\Delta H_{0\text{K}} = 10.3$  kcal/mol (implicitly assuming that the dissociation correlates adiabatically to the ground electronic states of the two products), conservation of energy (see eq 7) requires that the sum of the internal energies of the two fragments,

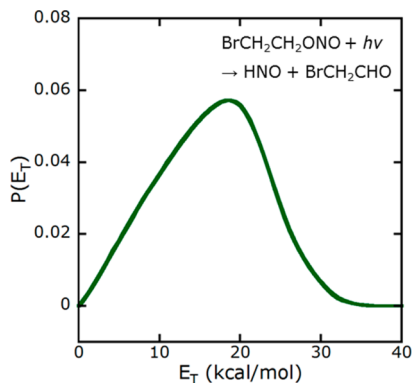


**Figure 5.** Photofragment recoil kinetic energy distribution,  $P(E_T)$ , of the HNO and BrCH<sub>2</sub>CHO fragments resulting from photoelimination of HNO from BrCH<sub>2</sub>CH<sub>2</sub>ONO at 193 nm. The  $P(E_T)$  is derived by forward convolution fitting of the signal at  $m/e = 31$  (HNO<sup>+</sup>).

$E_{\text{int}}(\text{HNO}) + E_{\text{int}}(\text{BrCH}_2\text{CHO})$ , lie in a range from 107 to 140 kcal/mol. The dissociation limit for HNO is 47.0 kcal/mol,<sup>43</sup> leading to the products H + NO with no barrier above the endoergicity.<sup>44</sup> We estimate the dissociation limit of BrCH<sub>2</sub>CHO to be no less than the endoergicity of transformation to Br + CH<sub>2</sub>CHO,  $\Delta H_{0\text{K}} = 60.3$  kcal/mol. (The transformation to CH<sub>2</sub>Br + CHO has a greater endoergicity, 78.5 kcal/mol; the transformation to HBr + ketene (H<sub>2</sub>CCO) has a transition state 62 kcal/mol above BrCH<sub>2</sub>CHO.) Any photodissociation event imparting greater than 47.0 + 60.3 = 107.3 kcal/mol of vibrational energy to the HNO and BrCH<sub>2</sub>CHO fragments must therefore lead to secondary dissociation of at least one of them. Lesser amounts of vibrational energy can also lead to secondary dissociation if the energy is, by chance, partitioned mainly into one fragment. Although the available  $E_{\text{int}}$  is always greater than 107 kcal/mol, an unknown fraction of the total is partitioned into rotational energy, which (to first order) cannot contribute to dissociation. We are unable to assess the amount of partitioning to rotational energy. Because there must be nonzero rotational energy, however, we conclude that not every primary photodissociation to HNO + BrCH<sub>2</sub>CHO must lead to secondary dissociation, but secondary dissociation of one fragment is energetically allowed if  $E_{\text{rot}}$  is low.

**3.2.3. Primary Photodissociation Leading to NO + BrCH<sub>2</sub>CH<sub>2</sub>O.** Photolysis to NO + alkoxy is a standard product channel for alkyl nitrites. The NO + BrCH<sub>2</sub>CH<sub>2</sub>O channel in this molecule was previously observed in studies at 193 nm and at 351/355 nm. We characterize this channel using data collected at  $m/e = 30$  (NO<sup>+</sup>, H<sub>2</sub>CO<sup>+</sup>) at several synchrotron energies below and above the 10.89 eV<sup>45,46</sup> ionization threshold of H<sub>2</sub>CO, another product of mass 30 (the ionization threshold of the major product, NO, is 9.26 eV<sup>47</sup>). Figure 6 shows TOF spectra and our forward convolution fits using 9.845 and 11.06 eV photoionization; in the Supporting Information we include the data and fits at 10.5, 10.84, and 11.27 eV. (The rising signal at long times, which is not from photofragments, is discussed in Section 3.1.) The contribution of primary NO photofragments is a sharp signal represented by the solid blue line peaking near 30 μs. Given in Figure 7 is the  $P(E_T)$  of this dissociation, indicating that the kinetic energy release extends from ~20 kcal/mol to ~45 kcal/mol, peaking near 33 kcal/mol. This is essentially identical to the  $P(E_T)$  of the previous study at 193

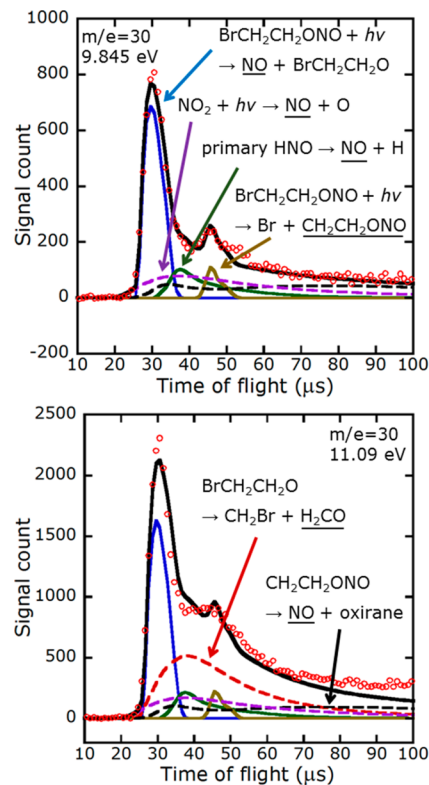


**Figure 6.** TOF spectrum of the signal at  $m/e = 30$  (NO<sup>+</sup>, H<sub>2</sub>CO<sup>+</sup>) at photoionization energies of 9.845 eV (upper) and 11.09 eV (lower). The sharply peaked signal near 30 μs is from primary O–NO bond photofission in BrCH<sub>2</sub>CH<sub>2</sub>ONO and is fitted by the solid blue line. Data and fits at other energies are provided in the Supporting Information. Contributions to the signal are the H<sub>2</sub>CO product of BrCH<sub>2</sub>CH<sub>2</sub>O (red dashed line, Section 3.5.1, visible only at high photon energy); secondary dissociation of HNO formed by photoelimination from BrCH<sub>2</sub>CH<sub>2</sub>ONO (solid green line peaking near 40 μs, Supporting Information); dissociative ionization of CH<sub>2</sub>CH<sub>2</sub>ONO radicals that are stable to secondary dissociation (solid brown line peaking near 45 μs, Section 3.2.1); the NO product of CH<sub>2</sub>CH<sub>2</sub>ONO (black dashed line, Section 3.3.2); and photodissociation of NO<sub>2</sub> formed with high internal energy from CH<sub>2</sub>CH<sub>2</sub>ONO (purple dashed line, Section 3.3.1).

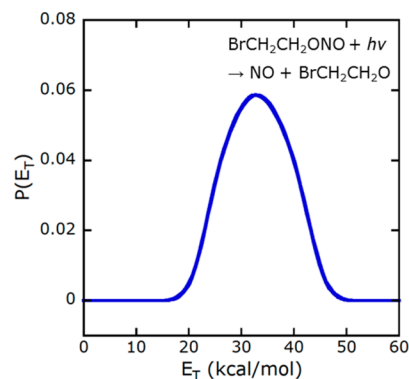


**Figure 7.** Photofragment recoil kinetic energy distribution,  $P(E_T)$ , of the NO + BrCH<sub>2</sub>CH<sub>2</sub>O resulting from primary photodissociation. The  $P(E_T)$ , peaking near 35 kcal/mol, is derived by forward convolution fitting of the signal near 35 μs in the data at  $m/e = 30$  shown in Figure 6. The TOF distribution predicted by this  $P(E_T)$  is shown as the solid blue line in that figure.

nm, differing from it by  $\sim 3$  kcal/mol in the peak position and in the length of the tail of the distribution at higher energies.

Other contributions to the data in Figure 6 are a strong, broad signal of  $\text{H}_2\text{CO}$  formed by secondary dissociation of  $\text{BrCH}_2\text{CH}_2\text{O}$  (dashed red line with a maximum near  $40 \mu\text{s}$ , only at  $11.09 \text{ eV}$ , Section 3.5.1); primary  $\text{HNO}$  undergoing secondary dissociation to  $\text{H} + \text{NO}$  (solid green line, Supporting Information); the  $\text{NO}$  product of secondary dissociation of  $\text{CH}_2\text{CH}_2\text{ONO}$  to  $\text{NO} + \text{oxirane}$  (dashed black curve, Section 3.3.2); an  $\text{NO}$  product formed by photodissociation of  $\text{NO}_2$ , a secondary product of  $\text{CH}_2\text{CH}_2\text{ONO}$  radicals (dashed purple line, Section 3.3.1); and dissociative ionization of  $\text{CH}_2\text{CH}_2\text{ONO}$  radicals that are stable to secondary dissociation (bimodal solid brown line near  $47 \mu\text{s}$ , discussed presently). No other fragment has a sharply peaked neutral flight time near  $47 \mu\text{s}$ , so we deduce that the sharply peaked signal in that region must be from dissociative ionization of stable  $\text{CH}_2\text{CH}_2\text{ONO}$ .

The TOF distribution of the  $\text{CH}_2\text{CH}_2\text{ONO}$  channel is derived using the portion of the  $\text{C}-\text{Br}$  photofission  $P(E_T)$  that is predicted, by our angular momentum model, to produce  $\text{CH}_2\text{CH}_2\text{ONO}$  radicals with less vibrational energy than the dissociation threshold. In Figure 2, this portion is represented by a black dashed line. The fit is remarkably good, given the assumptions of Section 3.2.1. There is some signal at slightly longer flight times than the fitted peak, near  $53 \mu\text{s}$ , which is not accounted for by the model; this signal is easily explained by supposing that some of the primary  $\text{Br}$  is likely produced as spin-orbit excited  $\text{Br}(^2\text{P}_{1/2})$ , and any stable  $\text{CH}_2\text{CH}_2\text{ONO}$  cofragments to these  $\text{Br}$  would, by conservation of energy, have lower  $E_T$  and longer flight times.

The internal energy of the  $\text{BrCH}_2\text{CH}_2\text{O}$  cofragment to primary  $\text{NO}$  photoproduct depends in part, by conservation of energy, on the rotational and vibrational energy of the departing  $\text{NO}$  fragment. Wang et al. gave a thorough assessment of these energetic sinks in the previous report, concluding that the average  $E_{\text{int}}(\text{NO})$  is likely on the order of  $30.0 \text{ kcal/mol}$ . Given this value, the  $P(E_T)$  of Figure 7, and  $\Delta H_{0\text{K}} = 39.0$ , we find that the  $E_{\text{int}}$  of  $\text{BrCH}_2\text{CH}_2\text{O}$  fragments fall in a range from  $\sim 30 \text{ kcal/mol}$  to  $\sim 55 \text{ kcal/mol}$ . These radicals therefore certainly can access the dissociation channels leading to  $\text{CH}_2\text{Br} + \text{H}_2\text{CO}$  and to  $\text{H}$  loss (as in the previous study), but higher-barrier products such as  $\text{HBr} + \text{vinoxy}$ ,  $\text{Br} + \text{oxirane}$ , and  $\text{Br} + \text{acetaldehyde}$  are far less favorable. In the Supporting Information we discuss evidence of a very small branching to  $\text{HBr} + \text{vinoxy}$  from  $\text{BrCH}_2\text{CH}_2\text{O}$ .

### 3.3. Secondary Dissociation of $\text{CH}_2\text{CH}_2\text{ONO}$ Radicals.

**3.3.1. The  $\text{NO}_2 + \text{Ethene}$  Channel.** Secondary dissociation of  $\text{CH}_2\text{CH}_2\text{ONO}$  radicals to  $\text{NO}_2 + \text{ethene}$  is characterized by data collected at  $m/e = 28$  ( $\text{CH}_2\text{CH}_2^+$ ) and  $m/e = 46$  ( $\text{NO}_2^+$ ), both with a synchrotron energy of  $10.84 \text{ eV}$ . The TOF data for both masses are shown in Figure 8. The data are fitted solely by this channel (solid black line), with no other contributions, because in this system  $\text{NO}_2$  and ethene are formed exclusively as cofragments. (Our data show no evidence of dissociative ionization of stable  $\text{CH}_2\text{CH}_2\text{ONO}$  radicals to either ion.) In fitting the data, we used only the portion of the primary  $\text{C}-\text{Br}$  photofission  $P(E_T)$  leading to unstable radicals, that is, the sum of the red-dashed and blue-dashed contributions in Figure 2.

The data evince an asymmetric  $I(\theta)$ : there is backward-scattering of the  $\text{NO}_2$  fragments and forward-scattering of the ethene fragments. To obtain a first approximation to the true  $I(\theta)$ , we employed the angular momentum model of Brynteson and Butler,<sup>42</sup> which predicts the speed and angular distributions

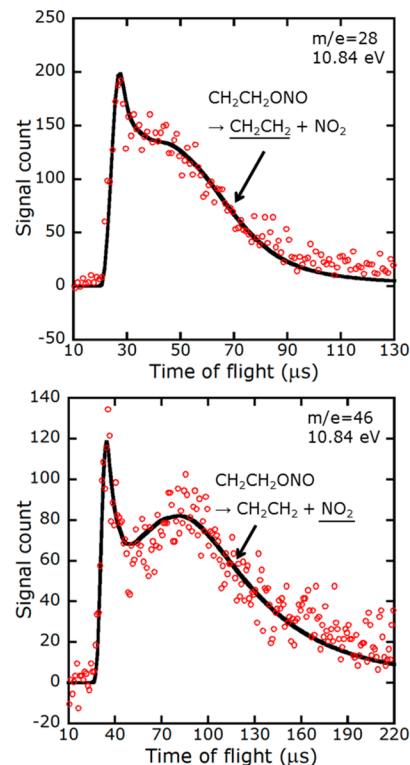


**Figure 8.** TOF spectra and forward convolution fits of  $m/e = 28$  ( $\text{CH}_2\text{CH}_2^+$ , top) and  $m/e = 46$  ( $\text{NO}_2^+$ , bottom) at a photoionization energy of  $10.84 \text{ eV}$ . These two species are formed exclusively as cofragments from secondary dissociation of  $\text{CH}_2\text{CH}_2\text{ONO}$ . The fitting of this channel is explained in the text.

of fragments of a dissociating species (here,  $\text{CH}_2\text{CH}_2\text{ONO}$ ) based on a calculation of its time-dependent angular velocity. The complete results of the model are provided in the Supporting Information; in sum, dissociation of  $\text{CH}_2\text{CH}_2\text{ONO}$  was predicted to strongly favor forward-scattering of ethene. Using this prediction as a template, we fitted the data at  $m/e = 28$  by iteratively adjusting both the  $I(\theta)$  and the  $P(E_T)$  for this dissociation. The derived  $P(E_T)$  and  $I(\theta)$  are shown in Figure 9, with the  $P(E_T)$  plotted as a solid black line. The fit to the data is shown in the top frame of Figure 8.

The  $\text{NO}_2^+$  data are not well-fitted by the total  $P(E_T)$  of Figure 9. However, a good fit is obtained by slightly decreasing the  $P(E_T)$  at low values of  $E_T$ . The adjusted  $P(E_T)$  is plotted as the dashed black line in the lower frame of Figure 9; it differs from the total  $P(E_T)$  only for  $E_T < 14 \text{ kcal/mol}$ . The fit to the data at  $m/e = 46$  given by this adjusted  $P(E_T)$  is shown in the lower frame of Figure 8. The necessity of this “adjustment” indicates that some of the  $\text{NO}_2$  fragments formed with low kinetic energy cannot be detected as  $\text{NO}_2^+$  but rather are lost to another process. Booth et al.<sup>48</sup> and Butler et al.<sup>49</sup> observed that  $\text{NO}_2$  fragments formed with high internal energy can photodissociate at  $193 \text{ nm}$  to form  $\text{NO} + \text{O}$ ; the  $P(E_T)$  for this photodissociation was determined in ref 49. We infer that the same process occurs here: some  $\text{NO}_2$  fragments formed with low kinetic energy have sufficient internal energy to undergo photodissociation, and thus cannot be detected as  $\text{NO}_2^+$ . The  $\text{NO}$  product of this photodissociation is observed as  $\text{NO}^+$  in the fits at  $m/e = 30$  of Figure 6. The contribution due to this channel is represented by the dashed purple line in that figure. Its TOF distribution was determined by forward convolution using, for primary photodissociation, the portion

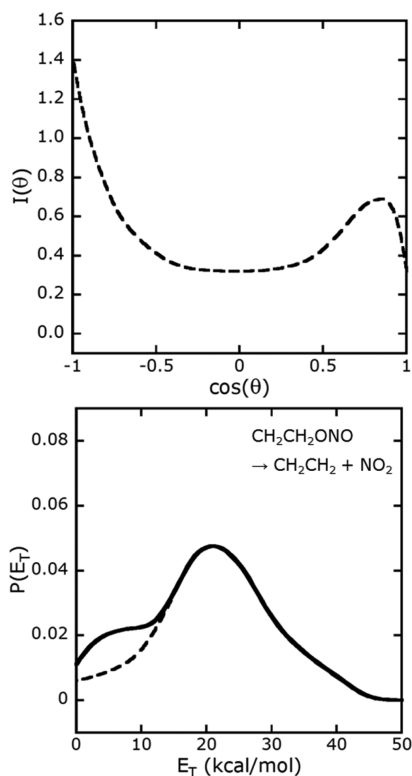


**Figure 9.** Angular distribution,  $I(\theta)$ , and product recoil kinetic energy distribution,  $P(E_T)$ , for the dissociation of  $\text{CH}_2\text{CH}_2\text{ONO}$  radicals to  $\text{NO}_2$  + ethene. Shown here is the  $I(\theta)$  for  $\text{NO}_2$ , which is backward-scattered; the angular distribution for its cofragment, ethene, is the mirror image of this distribution, where the mirror plane is  $\theta = 0^\circ$ . The total  $P(E_T)$ , shown in solid black line, gives the fit to the data at  $m/e = 28$  of Figure 8; the altered  $P(E_T)$ , shown in dashed black line but coinciding with the solid line above 14 kcal/mol, gives the fit to the data at  $m/e = 46$  of Figure 8. The fitting of this channel is explained in the text.

of the C–Br photofission  $P(E_T)$  leading to unstable  $\text{CH}_2\text{CH}_2\text{ONO}$  radicals; for secondary dissociation, the  $I(\theta)$  of Figure 9 and the portion of the  $P(E_T)$  of that figure leading to unstable  $\text{NO}_2$ , that is, the difference between the solid line and the dashed line; and for this photodissociation, an isotropic  $I(\theta)$  and the  $P(E_T)$  of Butler et al. (reproduced from ref 49 in the Supporting Information). The fit to the data at  $m/e = 30$  is quite satisfactory.

**3.3.2. The NO + Oxirane Channel.** Those  $\text{CH}_2\text{CH}_2\text{ONO}$  radicals with the highest vibrational energies can surmount a barrier of 24.1 kcal/mol from the trans conformer or 23.3 kcal/mol from the coplanar cis conformer to dissociate to NO + oxirane. Data taken at  $m/e = 44$  (oxirane cation) with a synchrotron energy of 10.84 eV are plotted in Figure 10, with the fit in black line. This channel is the only contributor of fragments of  $m/e = 44$ . The  $P(E_T)$  and  $I(\theta)$  derived by fitting the data are shown in Figure 11. The dissociation to NO + oxirane evinces a similar  $I(\theta)$  to that of dissociation to  $\text{NO}_2$  + ethene, with strongly forward-scattered oxirane. The fit to oxirane is verified by the fit at its dissociative ionization product,  $\text{CH}_3^+$ . The TOF distribution of oxirane fragments is shown as a black dashed line in the fit for  $m/e = 15$  ( $\text{CH}_3^+$ ) in Section 3.4.2; the predicted oxirane TOF distribution is found to agree with the data. The NO cofragment to this oxirane is detected as  $\text{NO}^+$  in the  $m/e = 30$  data of Figure 6; this channel

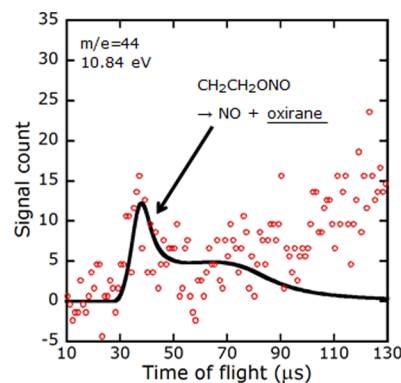


**Figure 10.** TOF spectrum and forward convolution fit of the signal at  $m/e = 44$  (oxirane cation) at a photoionization energy of 10.84 eV. Oxirane is formed exclusively from secondary dissociation of  $\text{CH}_2\text{CH}_2\text{ONO}$ .

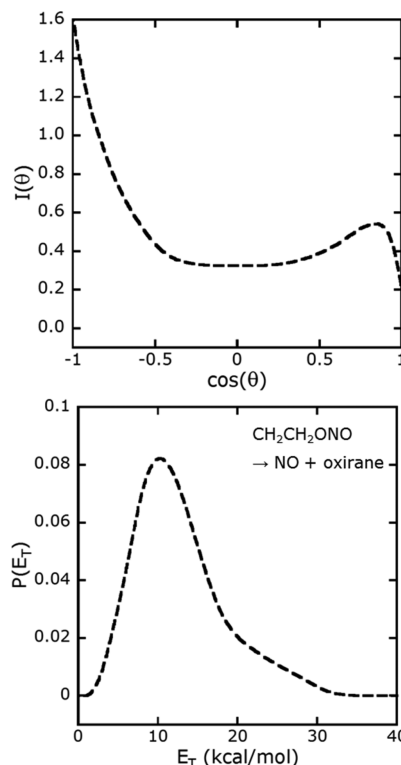


**Figure 11.** Angular distribution,  $I(\theta)$ , and product recoil kinetic energy distribution,  $P(E_T)$ , for the dissociation of  $\text{CH}_2\text{CH}_2\text{ONO}$  to NO + oxirane. Shown here is the  $I(\theta)$  for the NO fragment, which is backward-scattered; the  $I(\theta)$  for the oxirane is the mirror image of this distribution, where the mirror plane is  $\theta = 0^\circ$ . These distributions were derived by forward convolution fitting of the data at  $m/e = 44$  (oxirane cation) of Figure 10 and are supported by data at other masses as noted in the text.

is the major contributor to the NO signal at long flight times (aside from the background signal discussed in Section 3.1).

**3.3.3. The HNO + Vinyoxy Channel.** In this work we sought to determine whether the  $\text{CH}_2\text{CH}_2\text{ONO}$  radical undergoes unimolecular dissociation to form HNO + vinyoxy. The transformation is endoergic by 1.8 kcal/mol, as plotted in Figure 3. Data in support of this channel appear at  $m/e = 31$  ( $\text{HNO}^+$ , Figure 4) and at  $m/e = 43$  (vinyoxy cation, Figure 12). In both figures, our forward convolution fit for this HNO + vinyoxy channel is represented by the dashed red line, which has

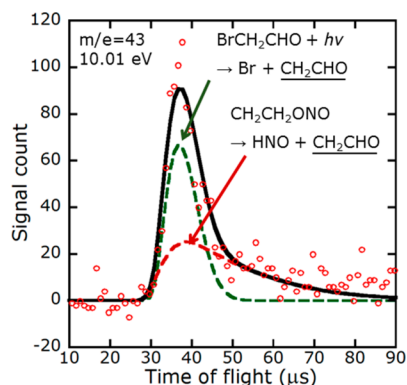


**Figure 12.** TOF spectrum of the signal at  $m/e = 43$  (vinoxy cation:  $\text{CH}_2\text{CHO}^+$ ) at a photoionization energy of 10.01 eV. Two contributions are observed: photodissociation of the  $\text{BrCH}_2\text{CHO}$  formed with primary photoelimination of HNO from  $\text{BrCH}_2\text{CH}_2\text{ONO}$  (green dashed line, Section 3.4.1), and secondary dissociation of  $\text{CH}_2\text{CH}_2\text{ONO}$  to HNO + vinoxy (red dashed line, Section 3.3.3). This fit does not represent all photodissociation of  $\text{BrCH}_2\text{CHO}$ , as some of the vinoxy produced in that process is unstable to further dissociation, and cannot be observed as  $\text{CH}_2\text{CHO}^+$ . For details, see the text.

a maximum near 30  $\mu\text{s}$  for HNO and near 35  $\mu\text{s}$  for vinoxy. We suppose that the barrier to this dissociation is not greater than the barrier to NO + oxirane (vide infra), so for these fits we use the portion of the primary C–Br photofission  $P(E_T)$  leading to radicals with enough vibrational energy to surmount the barrier to NO + oxirane, that is, the red curve of Figure 2. We also use the sideways-scattered secondary angular distribution of Figure 13. The  $P(E_T)$  for this dissociation is shown in Figure 14.

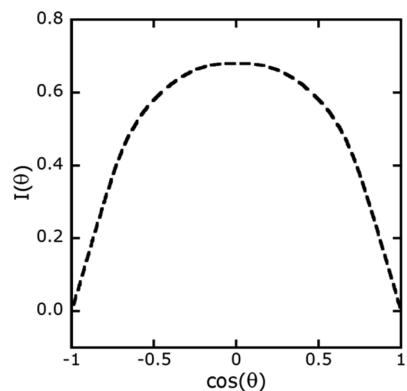


**Figure 13.** Angular distribution,  $I(\theta)$ , indicating “sideways-scattering”: the secondary dissociation event preferentially scatters both fragments perpendicularly to the velocity vector of the dissociating fragment.

Photodissociation of the precursor cannot lead to HNO +  $\text{BrCH}_2\text{CHO}$  with enough kinetic energy to account for the HNO signal at short flight times, as the TOF distributions of their  $\text{BrCH}_2\text{CHO}$  cofragments would not fit the data at  $m/e = 15$  (Section 3.4.2). Therefore, this HNO is from a secondary channel, and according to our analysis the only secondary channel that can lead to HNO from this precursor is the dissociation  $\text{CH}_2\text{CH}_2\text{ONO} \rightarrow \text{HNO} + \text{vinoxy}$ . The fit at  $m/e = 43$  is consistent with this conclusion. Moreover, since vinoxy from this channel is (by conservation of energy) formed with a low  $E_{\text{int}}$  it is stable to further dissociation, and can dissociatively ionize to  $\text{CH}_3^+$ . In the  $m/e = 15$  data of Section 3.4.2, the

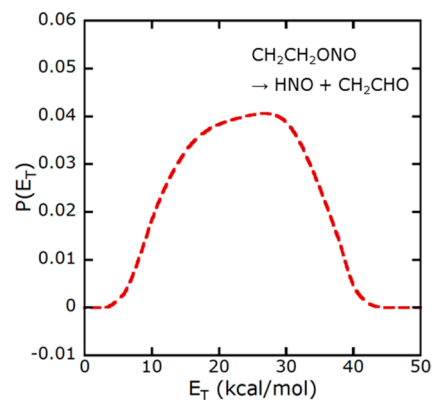


**Figure 14.** Recoil kinetic energy distribution,  $P(E_T)$ , for the secondary dissociation of  $\text{CH}_2\text{CH}_2\text{ONO}$  radicals to HNO + vinoxy. The dissociation follows the sideways-scattered angular distribution of Figure 13.

dashed red line with a maximum near 40  $\mu\text{s}$  represents the contribution of dissociative ionization of this source of vinoxy.

**3.4. Secondary Dissociation Following the HNO +  $\text{BrCH}_2\text{CHO}$  Primary Channel.** **3.4.1. Photodissociation of  $\text{BrCH}_2\text{CHO}$  to Produce Br + Vinoxy.** Figure 12 shows TOF data and forward convolution fits at  $m/e = 43$  (vinoxy,  $\text{CH}_2\text{CHO}^+$ ) taken with a synchrotron energy of 10.01 eV. We attribute most of the signal to photodissociation of nascent  $\text{BrCH}_2\text{CHO}$  to Br + vinoxy. This is, then, a two-photon process: the  $\text{BrCH}_2\text{CH}_2\text{ONO}$  precursor absorbs a 193 nm photon and dissociates to HNO +  $\text{BrCH}_2\text{CHO}$  (Section 3.2.2), whereupon the latter absorbs a 193 nm photon and dissociates to Br + vinoxy, analogously to the photodissociation of  $\text{ClCH}_2\text{CHO}$  at 193 nm to Cl + vinoxy.<sup>50</sup> (In the Supporting Information we explain why this signal should not be ascribed to a single-photon process.) The contribution from this source is represented by the green dashed line in Figure 12, and the photodissociation  $P(E_T)$  derived by forward convolution fitting of this contribution is shown by the red dashed line in Figure 15. This fit requires an  $I(\theta)$  peaking near  $90^\circ$ , plotted in Figure 13; that is, the Br and vinoxy fragments are scattered preferentially orthogonal to the velocity vector of the primary  $\text{BrCH}_2\text{CHO}$  fragments. The fit is supported by the data at  $m/e = 15$  ( $\text{CH}_3^+$ , Section 3.4.2). The other contribution to the data is secondary dissociation of  $\text{CH}_2\text{CH}_2\text{ONO}$  radicals to vinoxy + HNO (dashed red line, Section 3.3.3).

As in the 193 nm photodissociation of  $\text{ClCH}_2\text{CHO}$ , photodissociation events of  $\text{BrCH}_2\text{CHO}$  having lower kinetic energy release are expected to produce vinoxy radicals with sufficient  $E_{\text{vib}}$  to dissociate to  $\text{CH}_3 + \text{CO}$ . Br + vinoxy produced with lower  $E_T$  are observed in the data at  $m/e = 79$  ( $\text{Br}^+$ ) but not at  $m/e = 43$ . The total  $P(E_T)$  of Figure 15 thus includes a low- $E_T$  contribution leading to vibrationally unstable vinoxy, plotted as a dashed blue line with a maximum near 22 kcal/mol, which was derived by forward convolution fitting to the  $\text{Br}^+$  data of Figure 1. The fit to this channel in the  $\text{Br}^+$  data is shown as a dashed green line and is predicted by the entire  $\text{BrCH}_2\text{CHO}$  photodissociation  $P(E_T)$  of Figure 15, whereas the highest  $E_T$  values of this dissociation lead solely to stable vinoxy and are observed and fitted at  $m/e = 43$ . (Interestingly, the total  $P(E_T)$  resembles the one derived by Miller et al. in their study of the photodissociation of  $\text{ClCH}_2\text{CHO}$  to Cl + vinoxy at 193 nm.<sup>50</sup>)

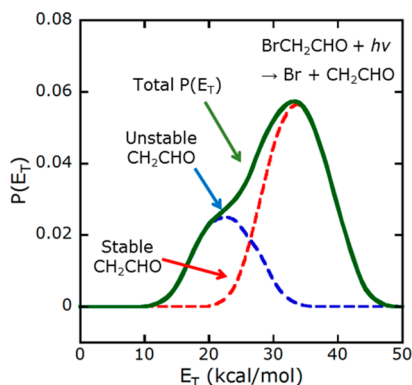


**Figure 15.** Recoil kinetic energy distribution,  $P(E_T)$ , for the photodissociation of  $\text{BrCH}_2\text{CHO}$  to  $\text{Br} + \text{vinyloxy}$  ( $\text{CH}_2\text{CHO}$ ). The dashed red line is obtained by fitting the data at  $m/e = 43$  (vinyloxy cation, dashed green line in Figure 12) and only represents kinetic energy release leading to vinyloxy that is stable to subsequent dissociation. The total  $P(E_T)$ , shown in solid green line, is obtained by fitting the data at  $m/e = 79$  ( $\text{Br}^+$ , dashed green line in Figure 1). The blue dashed line represents kinetic energy release leading to vinyloxy that undergoes subsequent dissociation to  $\text{CH}_3 + \text{CO}$  and is obtained by subtracting the red-dashed distribution from the solid-green distribution.

**3.4.2. Tertiary Dissociation of Vinyloxy.** The unstable vinyloxy indicated in Section 3.4.1 is expected, based on a previous study of  $\text{ClCH}_2\text{CHO}$ ,<sup>50</sup> to dissociate to  $\text{CH}_3 + \text{CO}$ . In Figure 16 we

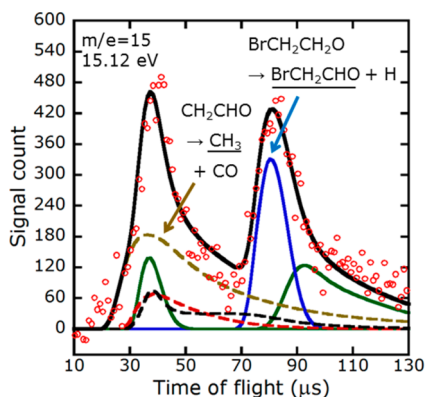


**Figure 16.** TOF spectrum of the signal at  $m/e = 15$  ( $\text{CH}_3^+$ ) at a synchrotron energy of 15.12 eV. The most important feature is the strong contribution of  $\text{CH}_3$  due to dissociation of vibrationally unstable vinyloxy (dashed brown line with a maximum near 40  $\mu\text{s}$ , Section 3.4.2). Other contributions are dissociative ionization of  $\text{BrCH}_2\text{CHO}$  from secondary dissociation of  $\text{BrCH}_2\text{CH}_2\text{O}$  (solid blue line peaking near 80  $\mu\text{s}$ , Section 3.5.3) and from photoelimination of  $\text{HNO}$  from  $\text{BrCH}_2\text{CH}_2\text{ONO}$  (solid green line with a maximum near 90  $\mu\text{s}$ , Section 3.2.2); dissociative ionization of vibrationally stable vinyloxy formed from photodissociation of  $\text{BrCH}_2\text{CHO}$  (solid red line, Section 3.4.1) and from secondary dissociation of  $\text{CH}_2\text{CH}_2\text{ONO}$  (dashed red line, Section 3.3.3); and dissociative ionization of vibrationally hot oxirane (dashed black line, Section 3.3.2).

present data acquired at  $m/e = 15$  ( $\text{CH}_3^+$ ) with a synchrotron energy of 15.12 eV, with which we characterize this channel. The kinetic energy release of this dissociation is not conclusively known, though in ref 50 it was found to be quite small. Our fit for this channel is shown as the dashed brown curve with a maximum near 40  $\mu\text{s}$  in Figure 16; for the kinetic energy release of this channel we used a roughly half-

normal distribution of standard deviation 5 kcal/mol, modified slightly to include a greater contribution of low  $E_T$ . The  $P(E_T)$  is shown in Figure 17. The TOF distribution of this channel

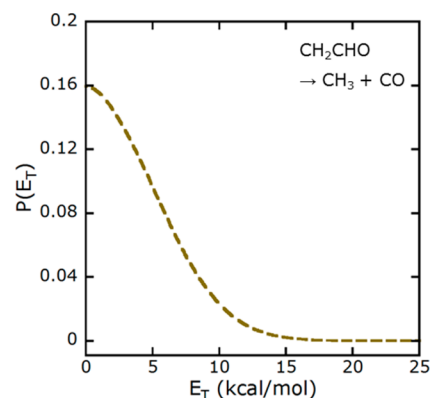


**Figure 17.** Product recoil kinetic energy distribution,  $P(E_T)$ , for the dissociation of vibrationally unstable vinyloxy,  $\text{CH}_2\text{CHO} \rightarrow \text{CH}_3 + \text{CO}$ . The distribution is approximately half-normal, with a standard deviation near 5 kcal/mol, and was derived by forward convolution fitting of the signal at  $m/e = 15$  ( $\text{CH}_3^+$ ) of Figure 16. The TOF distribution predicted by this  $P(E_T)$  is the dashed brown line in that figure.

was determined by forward convolution up to this “tertiary” dissociation, using for primary photodissociation the  $\text{HNO}$  photoelimination  $P(E_T)$  of Figure 5, which produces  $\text{BrCH}_2\text{CHO}$ ; for the secondary photodissociation, the low-kinetic energy portion of the  $\text{BrCH}_2\text{CHO}$  photodissociation  $P(E_T)$  of Figure 15 (plotted as a blue dashed line in that figure), which leads to vibrationally unstable vinyloxy, with the sideways-scattered  $I(\theta)$  of Figure 13; and, for the “tertiary” dissociation of vinyloxy, an isotropic  $I(\theta)$  and the  $P(E_T)$  of Figure 17. The fit to the fast edge of the  $m/e = 15$  data is overall quite satisfactory.

**3.4.3. Secondary Dissociation of HNO and Minor Dissociation Pathways of  $\text{BrCH}_2\text{CHO}$ .** We observed a small signal at  $m/e = 82$  ( $\text{H}^{81}\text{Br}^+$ ), which we attribute to photoelimination of  $\text{HBr}$  from  $\text{BrCH}_2\text{CHO}$ . We also observed some signal at  $m/e = 29$  ( $\text{HCO}$ ) arising largely from dissociative ionization of  $\text{BrCH}_2\text{CHO}$ ,  $\text{H}_2\text{CO}$ , and oxirane, and possibly also including photodissociation of  $\text{BrCH}_2\text{CHO}$  to  $\text{CH}_2\text{Br} + \text{HCO}$  (by analogy with other halogenated aldehydes<sup>51</sup>). Moreover, some of the  $\text{HNO}$  produced in the primary photodissociation of  $\text{BrCH}_2\text{CH}_2\text{ONO}$  has sufficient vibrational energy to dissociate to  $\text{H} + \text{NO}$ , detected as  $m/e = 30$  ( $\text{NO}^+$ , Figure 6). We include these data and some analysis of these product channels in the Supporting Information.

**3.5. Secondary Dissociation of the  $\text{BrCH}_2\text{CH}_2\text{O}$  Radical Formed from Primary O–NO Photofission.** **3.5.1. The  $\text{CH}_2\text{Br} + \text{H}_2\text{CO}$  Channel.** This channel is easily characterized using the data at  $m/e = 93$  ( $\text{CH}_2\text{Br}^+$ ), plotted in Figure 18. The signal is clearly forward–backward scattered with respect to the velocity vector of the primary  $\text{BrCH}_2\text{CH}_2\text{O}$  fragments, so we used an angular distribution of  $I(\theta)$  close to  $1/\sin(\theta)$  (truncated near  $\theta = 0^\circ$  and  $180^\circ$ ), shown in Figure 19. Figure 19 also shows the  $P(E_T)$  giving the fit of Figure 18; it extends from 0 to  $\sim 40$  kcal/mol, with a maximum near 15 kcal/mol. This  $P(E_T)$  is similar to the one derived by Wang et al. for this channel<sup>33</sup> but includes a contribution from higher  $E_T$ . However, the previous study assumed an isotropic  $I(\theta)$  for this dissociation, because they were unable to distinguish signal

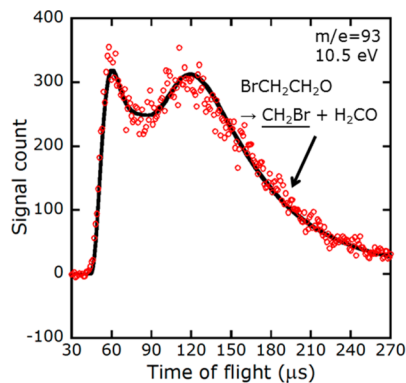


**Figure 18.** TOF spectrum and forward convolution fit of  $m/e = 93$  ( $\text{CH}_2\text{Br}^+$ ) signal at a photoionization energy of 10.5 eV. The signal is seen to be forward–backward scattered. The only contribution included here is  $\text{CH}_2\text{Br}$  formed by secondary dissociation of  $\text{BrCH}_2\text{CH}_2\text{O}$ . There is expected to be some  $\text{CH}_2\text{Br}$  formed by C–C bond photofission in  $\text{BrCH}_2\text{CHO}$ ; however, we were unable to fit the data well with this contribution included. We believe that the  $\text{CH}_2\text{Br}$  from  $\text{BrCH}_2\text{CH}_2\text{O}$  is the overwhelmingly dominant contributor.

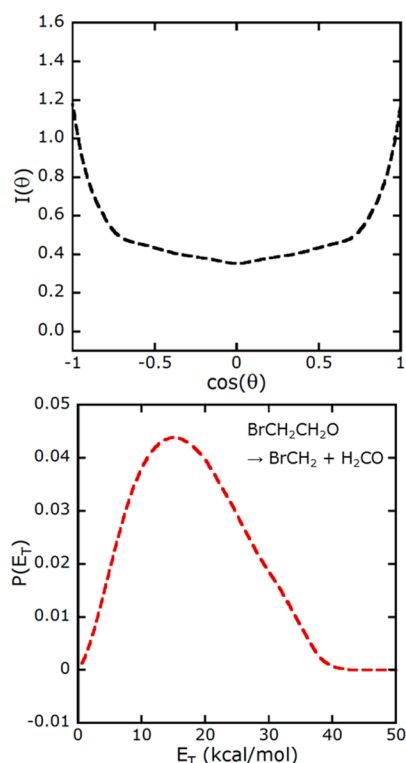


**Figure 19.** Angular distribution,  $I(\theta)$ , and product recoil kinetic energy distribution,  $P(E_T)$ , for the dissociation of  $\text{BrCH}_2\text{CH}_2\text{O}$  radicals to  $\text{CH}_2\text{Br} + \text{H}_2\text{CO}$ . The  $P(E_T)$  is derived by forward convolution fitting of the data at  $m/e = 93$  ( $\text{CH}_2\text{Br}^+$ ) of Figure 18.

due to backward-scattered  $\text{CH}_2\text{Br}$  fragments from signal due to photodissociation of clusters in the molecular beam. In this work, photoionization detection eliminates the contribution from the photodissociation of clusters, so all of the signal of Figure 18 arises from this  $\text{CH}_2\text{Br}$  channel. (We note in passing that the tail of the data at long time could include a contribution from the background signal described in Section 3.1. The background contribution, however, reaches its

maximum near 220  $\mu\text{s}$ , a time fairly well-separated from the more important data at 60–150  $\mu\text{s}$ .)

The momentum-matched formaldehyde cofragment of these  $\text{CH}_2\text{Br}$  fragments can be observed at  $m/e = 30$  ( $\text{NO}^+$ ,  $\text{H}_2\text{CO}^+$ ) at synchrotron energies above the 10.89 eV ionization threshold of  $\text{H}_2\text{CO}$ . In this experiment, the effective ionization threshold is somewhat lower, as the synchrotron radiation has nontrivial bandwidth ( $\sim 4\%$  full width at half-maximum) and the  $\text{H}_2\text{CO}$  is not vibrationally cold; thus, we used a nominal synchrotron energy as low as 9.845 eV, to collect data at  $m/e = 30$  with signal from  $\text{NO}^+$  but none from  $\text{H}_2\text{CO}^+$ , and up to 11.06 eV to guarantee a large signal from  $\text{H}_2\text{CO}^+$ . (At 11.06 eV, the photoionization cross section of  $\text{H}_2\text{CO}$  is  $\sim 11.4$  Mb,<sup>46</sup> much larger than that of the other major product,  $\text{NO}$ , which is  $\sim 3.2$  Mb.<sup>52,53</sup>) The data and fits at  $m/e = 30$  using ionization at 9.845 and 11.06 eV are shown in Figure 6; data and fits for other energies are presented in the Supporting Information. A contribution from the  $\text{H}_2\text{CO}$  cofragment of  $\text{CH}_2\text{Br}$ , drawn as a dashed red line with a maximum near 40  $\mu\text{s}$ , is clearly absent in the data at low synchrotron energy, but predictably increases with increasing energy. For these fits we also kept constant the relative intensities of contributions from different sources of  $\text{NO}$ , since we do not expect the photoionization cross section of  $\text{NO}$  from different sources to vary considerably over this energy range. The total fit describes the data well, supporting our assignment of the  $\text{CH}_2\text{Br} + \text{H}_2\text{CO}$   $P(E_T)$  and  $I(\theta)$ .

**3.5.2. Photodissociation of  $\text{CH}_2\text{Br}$ .** In the data of Figure 1 at  $m/e = 79$  ( $\text{Br}^+$ ), there is signal at incredibly short flight times, on the order of 40  $\mu\text{s}$ . To produce  $\text{Br}$ , a heavy fragment, with sufficient speed to have such a short flight time would require, by conservation of energy, more kinetic energy release (on the order of 80 kcal/mol) than is possible for single-photon dissociation of  $\text{BrCH}_2\text{CH}_2\text{ONO}$ . Consequently this signal must represent  $\text{Br}$  formed by a two-photon dissociation. It cannot arise from photodissociation of  $\text{BrCH}_2\text{CHO}$ , however, as there is no momentum-matched vinyloxy signal to this  $\text{Br}$ . Instead, we fit it as photodissociation of the  $\text{CH}_2\text{Br}$  formed by the pathway described in Section 3.5.1. The fit is presented in Figure 1 as a dashed purple line. The TOF distribution was predicted by the usual forward convolution fitting process using the entire primary O–NO  $P(E_T)$  of Figure 7, the entire  $P(E_T)$  and  $I(\theta)$  for secondary dissociation of  $\text{BrCH}_2\text{CH}_2\text{O}$  of Figure 19, and a tertiary photodissociation  $P(E_T)$  plotted in Figure 20 with an isotropic  $I(\theta)$ . The total fit including this contribution from photodissociation of  $\text{CH}_2\text{Br}$  is seen to be quite satisfactory.

The  $P(E_T)$  for this dissociation was estimated as follows. Reisler and co-workers have reported recoil kinetic energy distributions for the photodissociation of  $\text{CH}_2\text{Cl}$  at 312–214 nm, including a significant contribution of hot bands over part of this region.<sup>54–56</sup> The  $P(E_T)$  values at the shortest wavelengths (see Figure 6 in ref 54) can be approximated by a normal distribution with a maximum at  $\sim 53\%$  of the available energy (i.e., photon energy minus  $\Delta H_{0K}$ ) and a standard deviation of  $\sim 3500$   $\text{cm}^{-1}$ . Separately, others have found that in the photodissociation of both  $\text{CH}_3\text{Cl}$ <sup>57</sup> and  $\text{CH}_3\text{Br}$ <sup>58</sup> at 193 nm,  $\sim 96\%$  of the available energy is partitioned into  $E_T$ . Given this similarity in the photodissociation dynamics of  $\text{CH}_3\text{Cl}$  and  $\text{CH}_3\text{Br}$ , we make the bold assumption that  $\text{CH}_2\text{Br}$ , like  $\text{CH}_2\text{Cl}$ , will photodissociate with a kinetic energy release normally distributed about a mean of  $\sim 53\%$  of its available energy, with a standard deviation of  $\sim 3500$   $\text{cm}^{-1}$ . Since  $\Delta H_{0K}(\text{CH}_2-\text{Br}) = 79.2$  kcal/mol and the energy of a 193 nm photon is 147.8 kcal/mol, the available energy is at least 68.6 kcal/mol, and the

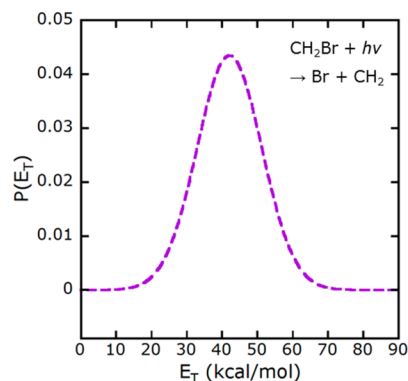


**Figure 20.** Photofragment recoil kinetic energy distribution,  $P(E_T)$ , used in the TOF prediction for the photodissociation  $\text{CH}_2\text{Br} + h\nu \rightarrow \text{Br} + \text{CH}_2$ . The  $P(E_T)$  is approximately a normal distribution centered at 42 kcal/mol with a standard deviation of 10 kcal/mol. It was derived by shifting the known  $P(E_T)$  of the analogous photodissociation of  $\text{CH}_2\text{Cl}$  to higher  $E_T$ , as more energy is available to  $\text{CH}_2\text{Br}$  than to  $\text{CH}_2\text{Cl}$ ; details are given in Section 3.5.2.

maximum of the  $P(E_T)$  occurs near  $(68.6 \text{ kcal/mol}) \times (53\%) = 36 \text{ kcal/mol}$ . We obtained a better fit by shifting this “guess”  $P(E_T)$  by 6 kcal/mol, increasing the mean to 42 kcal/mol; this shift may be justified by noting that the vibrational energy of the hot  $\text{CH}_2\text{Br}$  fragments can contribute to  $E_T$ . The final  $P(E_T)$ , shown in Figure 20, gives the fit of the dashed purple line in the  $m/e = 79$  data of Figure 1.

**3.5.3. The  $\text{BrCH}_2\text{CHO} + \text{H}$  Channel.**  $\text{BrCH}_2\text{CH}_2\text{O}$  radicals can undergo secondary dissociation via H loss, producing  $\text{H} + \text{BrCH}_2\text{CHO}$ . This channel was observed in both this study and the previous study by detecting the dissociative ionization products of  $\text{BrCH}_2\text{CHO}$ , which appear in much of the data of this report and at  $m/e = 29$  and  $m/e = 79$  in the previous report; in this study we were moreover able to detect the parent cation at  $m/e = 122$ . We include some further analysis of this pathway in the Supporting Information.

## 4. DISCUSSION

The work reported here continues a previous study that explored the photochemistry of  $\text{BrCH}_2\text{CH}_2\text{ONO}$  and its photofragment  $\text{BrCH}_2\text{CH}_2\text{O}$  using 200 eV electron bombardment ionization. Insofar as this work overlaps theirs, the two are essentially in agreement, with the sole exception of the dissociation of  $\text{BrCH}_2\text{CH}_2\text{O}$  to  $\text{CH}_2\text{Br} + \text{H}_2\text{CO}$ , which was fitted using an isotropic  $I(\theta)$  in the previous study but  $I(\theta)$  close to  $1/\sin(\theta)$  here.

**Nitrite Photochemistry.** A key new result of this work is the data and analysis at  $m/e = 31$  ( $\text{HNO}^+$ ), which indicates formation of HNO as a primary photodissociation product of  $\text{BrCH}_2\text{CH}_2\text{ONO}$  and as a secondary dissociation product of  $\text{CH}_2\text{CH}_2\text{ONO}$ . The appearance of HNO from an alkyl nitrite is typically ascribed to the kinetic disproportionation mechanism mentioned in the Introduction. There has been some debate in the literature regarding whether a monomeric nitrite can evolve HNO under collision-free conditions. Most relevant to the present study is that Bergmann and Huber,<sup>22</sup> in a laser-induced fluorescence experiment, observed HNO production from a molecular beam of methyl nitrite clusters ( $[\text{CH}_3\text{ONO}]_n$ ,  $n \approx 400\text{--}1000$ ) photoexcited at 365 nm, which they attributed entirely to disproportionation within the clusters. The HNO signal in this work, however, cannot be assigned to photodissociation within nitrite clusters. The ion signal at  $m/e = 31$

(Figure 4) and  $m/e = 30$  (Figure 6) near 40  $\mu\text{s}$ , and at  $m/e = 15$  (Figure 16) and  $m/e = 29$  (Supporting Information) near 100  $\mu\text{s}$ , is best explained as representing HNO and  $\text{BrCH}_2\text{CHO}$  formed as momentum-matched cofragments in the primary photodissociation of  $\text{BrCH}_2\text{CH}_2\text{ONO}$ . In addition, the ion signal at  $m/e = 31$  (Figure 4) near 30  $\mu\text{s}$  is best explained as HNO formed in the secondary dissociation of  $\text{CH}_2\text{CH}_2\text{ONO}$ , with a vinoxy cofragment observed as ion signal at  $m/e = 43$  (Figure 12) near 45  $\mu\text{s}$  and at  $m/e = 15$  (Figure 16) near 40  $\mu\text{s}$ .

Comparing our conclusions on HNO to the conclusions of Bergmann and Huber, it might be inferred that alkyl nitrites photoexcited in the absorption band near 200 nm can access a unimolecular photoelimination channel leading to HNO, whereas no such channel occurs upon excitation near 350 nm. It is not clear whether this dissociation would occur through the excited state or following internal conversion to the ground state. It is also possible, though perhaps less likely, that a photodissociation channel leading to HNO is accessible exclusively in substituted alkyl nitrites. Further study is required to explore these questions.

**Mechanism of Dissociation of  $\text{CH}_2\text{CH}_2\text{ONO}$  to HNO + Vinoxy.** Our data and calculations show multiple dissociation pathways of the  $\text{CH}_2\text{CH}_2\text{ONO}$  radical. On the basis of the barrier heights and  $P(E_{\text{vib}})$  of Figure 3, statistical transition-state theory would predict overwhelming branching to the  $\text{NO}_2 + \text{ethene}$  products, with some small contribution of  $\text{NO} + \text{oxirane}$  and practically no contribution from  $\text{HNO} + \text{vinoxy}$ . The data do show strong signal due to  $\text{NO}_2$  and ethene, but the signal due to  $\text{HNO} + \text{vinoxy}$  is unexpectedly competitive with the signal due to  $\text{NO} + \text{oxirane}$ . In this section we claim that the dissociation to HNO occurs through a non-intrinsic reaction coordinate (non-IRC) mechanism that circumvents the high-energy conventional transition state along an IRC used in statistical transition state theories.

Two conceptually similar dissociations are  $\text{CH}_3\text{ONO} \rightarrow \text{HNO} + \text{H}_2\text{CO}$ , the subject of recent calculations by Zhu et al.,<sup>13,59</sup> Isegawa et al.,<sup>60</sup> and Homayoon and Bowman;<sup>14,15</sup> and  $\text{CH}_3\text{CH}_2\text{ONO} \rightarrow \text{HNO} + \text{CH}_3\text{CHO}$ , which was approached theoretically by Liu et al.<sup>25</sup> and experimentally by Prozument et al.<sup>24</sup> In both cases there is a conventional transition state (TS) to HNO that is a few kilocalories per mole higher than the dissociation threshold to NO; the highest-energy TS of Figure 3 is analogous. However, the studies of Zhu et al., Isegawa et al., and Prozument et al. also suggest “roaming” pathways leading to HNO, with an energetic barrier approximately equal to the dissociation threshold to NO. In these pathways there is frustrated dissociation of the RO–NO bond, whereupon the RO and NO fragments orbit one another: the molecule samples a large region of its potential energy surface at no energetic penalty, until the geometric trajectory falls into an exoergic well. The existence of such a “roaming” pathway in  $\text{CH}_2\text{CH}_2\text{ONO}$  would explain our observation that dissociation to HNO + vinoxy is competitive with dissociation to NO + oxirane; this hypothetical feature is labeled “RTS?” in Figure 3. (The connection of RTS? to the HNO + vinoxy van der Waals well is inspired by the result of Homayoon and Bowman that  $\text{CH}_3\text{ONO}$  can dissociate to HNO via an  $\text{HNO} + \text{H}_2\text{CO}$  vdW complex, but it is otherwise purely speculative.)

The analogy between  $\text{CH}_2\text{CH}_2\text{ONO}$  and the closed-shell nitrites is imperfect because the NO channel in  $\text{CH}_2\text{CH}_2\text{ONO}$  is exoergic with a high barrier, while in methyl and ethyl nitrite it is endoergic with negligible barrier above the endoergicity. The presence of a barrier to dissociation, from which both the

NO and HNO pathways are exoergic, is suggestive of a bifurcation in the potential energy surface in the vicinity of that TS: having surmounted (or nearly surmounted) the dissociation barrier, the molecule may follow nuclear trajectories leading from the TS toward either the NO + oxirane well or the hypothesized NO roaming region. Numerous examples of potential energy surfaces with bifurcations of this type are now known, including unimolecular rearrangements and dissociations<sup>61,62</sup> as well as bimolecular reactions.<sup>63,64</sup> The common feature of such systems is that the dynamics in the vicinity of the transition state, not the IRC, control the reactive trajectory.

In the case of CH<sub>2</sub>CH<sub>2</sub>ONO, such a bifurcation could be understood intuitively by supposing (following the argument of ref 63) that the molecule's vibrational energy is not efficiently channeled into the O–NO stretching coordinate, so the orthogonal vibrational modes retain much of the vibrational energy and avoid the bond-breaking pathway. One feature of the experimental results provide a modicum of support for this interpretation. While the IRC trajectory toward NO + oxirane entails direct repulsion along the O–NO bond, the hypothetical non-IRC trajectory entails moving the NO in a sideways direction to abstract an H atom. Such a non-IRC pathway, then, might be expected to scatter HNO fragments sideways with respect to the NO fragments, as was observed in these experiments. A direct dynamics calculation beginning with the electronically excited precursor is required to fully characterize the angular distribution of the products from this hypothesized roaming channel.

**Characterization of Multiphoton Dissociations.** Our data evince significant multiphoton effects, namely, in the photodissociations of BrCH<sub>2</sub>CHO to Br + vinoxy, of CH<sub>2</sub>Br to Br + CH<sub>2</sub>, and of NO<sub>2</sub> to NO + O. The photodissociation of these species has serendipitously allowed us to roughly characterize the photochemistry of BrCH<sub>2</sub>CHO and CH<sub>2</sub>Br at 193 nm, and to show that vibrationally excited CH<sub>2</sub>CH<sub>2</sub>ONO can evolve NO<sub>2</sub> with the requisite internal energy to undergo photodissociation. In fitting these channels we have drawn parallels to previous work on the photodissociation of ClCH<sub>2</sub>CHO and ClCH<sub>2</sub>, and the agreement of these fits with the data is quite good. It would be interesting to verify the  $P(E_T)$ s derived here by conducting a single-photon experiment on photodissociation of vibrationally cold BrCH<sub>2</sub>CHO monomers and CH<sub>2</sub>Br.

## ■ ASSOCIATED CONTENT

### 📄 Supporting Information

The Supporting Information is available free of charge on the ACS Publications website at DOI: 10.1021/acs.jpca.5b12669.

TOF distributions of background signal at  $m/e = 29$ , 30, and 44, and TOF data at these masses after background subtraction. Data and fits for  $m/e = 30$  at 10.5, 10.84, and 11.27 eV. Discussion of: secondary dissociation of vibrationally excited HNO; ancillary data and possible sources of  $m/e = 29$  and  $m/e = 82$ , including the lack of CH<sub>2</sub>Br signal due to BrCH<sub>2</sub>CHO; and the appearance of BrCH<sub>2</sub>CHO<sup>+</sup> at  $m/e = 122$ . Statistical justification for rejecting the hypothesis that BrCH<sub>2</sub>CHO undergoes secondary dissociation due to vibrational excitation. Predicted speed and angular distributions for secondary dissociation of CH<sub>2</sub>CH<sub>2</sub>ONO.  $P(E_T)$  used for the photodissociation of NO<sub>2</sub>. Cartesian coordinates of the minima and transition states of CH<sub>2</sub>CH<sub>2</sub>ONO. (PDF)

## ■ AUTHOR INFORMATION

### Corresponding Author

\*E-mail: L-Butler@uchicago.edu. Phone: 773-702-7206.

### Notes

The authors declare no competing financial interest.

## ■ ACKNOWLEDGMENTS

This work was supported by the Chemical Sciences, Geosciences and Biosciences Division, Office of Basic Energy Sciences, Office of Science, U.S. Department of Energy, under Grant No. DE-FG02-92ER14305 (L.J.B.). T.D.R. was supported by the Arnold and Mabel Beckman Foundation as a Beckman Scholar. Synchrotron beam time and additional funding were provided by the National Synchrotron Radiation Research Center. We thank Prof. Y.-P. Lee for the use of laboratory facilities and reagents for the synthesis and storage of BrCH<sub>2</sub>CH<sub>2</sub>ONO. We are deeply grateful for the assistance of W.-J. Huang, Dr. Y.-L. Sun, Dr. M. D. Brynteson, and Dr. L. Wang in using and maintaining the experimental apparatus and in collecting data. Dr. Brynteson also provided valuable advice regarding the angular momentum model used to predict angular distributions in this report. Dr. S. Li, a visiting scientist in our group, identified the “out-of-plane cis” conformer of CH<sub>2</sub>CH<sub>2</sub>ONO.

## ■ REFERENCES

- (1) Wayne, R. P. *Chemistry of Atmospheres*, 3rd ed.; Oxford University Press: Oxford, U.K., 2000.
- (2) Calvert, J. G.; Pitts, J. N., Jr. *Photochemistry*; Wiley: New York, 1966.
- (3) McMillan, G. R.; Kumari, J.; Snyder, D. L. The Photolysis and Photooxidation of Alkyl Nitrites. In *Chemical Reactions in Urban Atmospheres*; Tuesday, C. S., Ed.; Elsevier: New York, 1971; pp 35–43.
- (4) Dixon, R. N.; Rieley, H. State-selected Photodissociation Dynamics of HONO ( $\tilde{A}^1A''$ ): Characterization of the NO Fragment. *J. Chem. Phys.* **1989**, *91*, 2308–2320.
- (5) Vasudev, R.; Zare, R. N.; Dixon, R. N. Dynamics of Photodissociation of HONO at 369 nm: Motional Anisotropy and Internal State Distribution of the OH Fragment. *Chem. Phys. Lett.* **1983**, *96*, 399–402.
- (6) Vasudev, R.; Zare, R. N.; Dixon, R. N. State-Selected Photodissociation Dynamics: Complete Characterization of the OH Fragment Ejected by the HONO  $\tilde{A}$  State. *J. Chem. Phys.* **1984**, *80*, 4863–4878.
- (7) Brühlmann, U.; Dubs, M.; Huber, J. R. Photodissociation of Methylnitrite: State Distributions, Recoil Velocity Distribution, and Alignment Effects of the NO( $X^2\Pi$ ) Photofragment. *J. Chem. Phys.* **1987**, *86*, 1249–1257.
- (8) Benoist d'Azy, O.; Lahmani, F.; Lardeux, C.; Solgadi, D. State-Selective Photochemistry: Energy Distribution in the NO Fragment after Photodissociation of the CH<sub>3</sub>ONO  $n\pi^*$  State. *Chem. Phys.* **1985**, *94*, 247–256.
- (9) Lahmani, F.; Lardeux, C.; Solgadi, D. Rotational and Electronic Anisotropy in NO  $X^2\Pi$  from the Photodissociation of CH<sub>3</sub>ONO. *Chem. Phys. Lett.* **1986**, *129*, 24–30.
- (10) Winniczek, J. W.; Dubs, R. L.; Appling, J. R.; McKoy, V.; White, M. G. A Multiphoton Ionization Study of the Photodissociation Dynamics of the S<sub>2</sub> State of CH<sub>3</sub>ONO. *J. Chem. Phys.* **1989**, *90*, 949–963.
- (11) Yin, H. M.; Sun, J. L.; Li, Y. M.; Han, K. L.; He, G. Z. Photodissociation Dynamics of the S<sub>2</sub> State of CH<sub>3</sub>ONO: State Distributions and Alignment Effects of the NO ( $X^2\Pi$ ) Photofragment. *J. Chem. Phys.* **2003**, *118*, 8248–8255.
- (12) Jacox, M. E.; Rook, F. L. Photodecomposition of Methyl Nitrite Trapped in Solid Argon. *J. Phys. Chem.* **1982**, *86*, 2899–2904.

- (13) Zhu, R. S.; Raghunath, P.; Lin, M. C. Effect of Roaming Transition States upon Product Branching in the Thermal Decomposition of  $\text{CH}_3\text{NO}_2$ . *J. Phys. Chem. A* **2013**, *117*, 7308–7313.
- (14) Homayoon, Z.; Bowman, J. M. Quasiclassical Trajectory Study of  $\text{CH}_3\text{NO}_2$  Decomposition via Roaming Mediated Isomerization Using a Global Potential Energy Surface. *J. Phys. Chem. A* **2013**, *117*, 11665–11672.
- (15) Bowman, J. M. Roaming. *Mol. Phys.* **2014**, *112*, 2516–2528.
- (16) Schwartz-Lavi, D.; Bar, I.; Rosenwaks, S. Rotational Alignment and Non-Statistical  $\Lambda$  Doublet Population in NO Following  $(\text{CH}_3)_3\text{CONO}$  Photodissociation. *Chem. Phys. Lett.* **1986**, *128*, 123–126.
- (17) Schwartz-Lavi, D.; Rosenwaks, S. Scalar and Vectorial Properties in the Photodissociation of tert-Butyl Nitrite from the S1 and S2 States. *J. Chem. Phys.* **1988**, *88*, 6922–6930.
- (18) Fitzmaurice, D. J.; Frei, H. Electronic Absorption of Alkyl Nitrite Radicals in the 300–700 nm Region. *Chem. Phys. Lett.* **1992**, *192*, 166–172.
- (19) Furlan, A. Photodissociation of an Alkyl Nitrite at a Liquid Surface: Flight-time Distributions of NO and HNO. *Chem. Phys. Lett.* **1999**, *309*, 157–164.
- (20) Mátyus, E.; Magyarfalvi, G.; Tarczay, G. Conformers and Photochemistry of Propyl Nitrites: A Matrix Isolation Study. *J. Phys. Chem. A* **2007**, *111*, 450–459.
- (21) Müller, R.-P.; Murata, S.; Nonella, M.; Huber, J. R. HNO, an Intermediate in (Light-induced) Rearrangement Reactions of Nitrosoxy Compounds and Nitrosamines. *Helv. Chim. Acta* **1984**, *67*, 953–958.
- (22) Bergmann, K.; Huber, J. R. Photoinduced Bimolecular Reactions in Homogeneous  $[\text{CH}_3\text{ONO}]_n$  Clusters. *J. Phys. Chem. A* **1997**, *101*, 259–267.
- (23) Batt, L.; Milne, R. T. The Gas-Phase Pyrolysis of Alkyl Nitrites. IV. Ethyl Nitrite. *Int. J. Chem. Kinet.* **1977**, *9*, 549–565.
- (24) Prozument, K.; Suleimanov, Y. V.; Buesser, B.; Oldham, J. M.; Green, W. H.; Suits, A. G.; Field, R. W. A Signature of Roaming Dynamics in the Thermal Decomposition of Ethyl Nitrite: Chirped-Pulse Rotational Spectroscopy and Kinetic Modeling. *J. Phys. Chem. Lett.* **2014**, *5*, 3641–3648.
- (25) Liu, Y.; Li, X.; Tian, G.; Li, X.; Sun, Z. Theoretical Study on the Reaction Mechanism of  $\text{CH}_3\text{CH}_2\text{O}$  Radical with NO. *Comput. Theor. Chem.* **2014**, *1032*, 84–89.
- (26) Von Glasow, R.; Crutzen, P. J. Tropospheric Halogen Chemistry. In *The Atmosphere*; Keeling, R. F., Ed.; Oxford University Press: Oxford, U.K., 2007; pp 21–64.
- (27) Knipping, E. M.; Lakin, M. J.; Foster, K. L.; Jungwirth, P.; Tobias, D. J.; Gerber, R. B.; Dabdub, D.; Finlayson-Pitts, B. J. Experiments and Simulations of Ion-Enhanced Interfacial Chemistry on Aqueous NaCl Aerosols. *Science* **2000**, *288*, 301–306.
- (28) Thornton, J. A.; Kercher, J. P.; Riedel, T. P.; Wagner, N. L.; Cozic, J.; Holloway, J. S.; Dube, W. P.; Wolfe, G. M.; Quinn, P. L.; Middlebrook, A. M.; Alexander, B.; Brown, S. S. A Large Atomic Chlorine Source Inferred from Mid-continental Reactive Nitrogen Chemistry. *Nature* **2010**, *464*, 271–274.
- (29) Calvert, J. G.; Atkinson, R.; Kerr, J. A.; Madronich, S.; Moortgat, G. K.; Wallington, T. J. *The Mechanisms of Atmospheric Oxidation of the Alkenes*; Oxford University Press: New York, 2000.
- (30) Nakata, M.; Shibuya, K.; Frei, H. Vibronic Excitation of Oxygen-Atom Transfer from  $\text{NO}_2$  to Ethylene by Long-Wavelength Visible Light in a Cryogenic Matrix. *J. Phys. Chem.* **1990**, *94*, 8168–8175.
- (31) Chhantyal-Pun, R.; Chen, M.-W.; Sun, D.; Miller, T. A. Detection and Characterization of Products from Photodissociation of  $\text{XCH}_2\text{CH}_2\text{ONO}$  ( $\text{X} = \text{F}, \text{Cl}, \text{Br}, \text{OH}$ ). *J. Phys. Chem. A* **2012**, *116*, 12032–12040.
- (32) Wang, L.; Lam, C.-S.; Chhantyal-Pun, R.; Brynteson, M. D.; Butler, L. J.; Miller, T. A. Imaging and Scattering Studies of the Unimolecular Dissociation of the  $\text{BrCH}_2\text{CH}_2\text{ONO}$  Radical from  $\text{BrCH}_2\text{CH}_2\text{ONO}$  Photolysis at 351 nm. *J. Phys. Chem. A* **2014**, *118*, 404–416.
- (33) Wang, L.; Scrape, P. G.; Roberts, T. D.; Joshi, P. P.; Butler, L. J. Competing C-Br and O-NO Photofission upon Excitation of  $\text{BrCH}_2\text{CH}_2\text{ONO}$  at 193 nm. *J. Phys. Chem. A* **2015**, *119*, 12005–12014.
- (34) Ratliff, B. J.; Alligood, B. W.; Butler, L. J.; Lee, S.-H.; Lin, J. J.-M. Product Branching from the  $\text{CH}_2\text{CH}_2\text{OH}$  Radical Intermediate of the OH + Ethene Reaction. *J. Phys. Chem. A* **2011**, *115*, 9097–9110.
- (35) Lin, J. J.; Chen, Y.; Lee, Y. Y.; Lee, Y. T.; Yang, X. Photodissociation Dynamics of  $\text{CH}_3\text{Cl}$  at 157.6 nm: Evidence for  $\text{CH}_2(\tilde{X}^3\text{B}_1/\tilde{a}^1\text{A}_1)+\text{HCl}$  Product Channels. *Chem. Phys. Lett.* **2002**, *361*, 374–382.
- (36) Lee, S.-H.; Lee, Y.-Y.; Lee, Y. T.; Yang, X. Photodissociation Dynamics of Propene at 157.6 nm: Kinetic Energy Distributions and Branching Ratios. *J. Chem. Phys.* **2003**, *119*, 827–838.
- (37) CMLAB2, version 6/93, modified by J. D. Myers. This is an interactive version built on the original cmlab2 program: Zhao, X. Ph.D. Dissertation, University of California, 1988.
- (38) Frisch, M. J.; Trucks, G. W.; Schlegel, H. B.; et al. *Gaussian 09*, Revision A.02; Gaussian, Inc: Wallingford, CT, 2009.
- (39) Schaftenaar, G.; Noordik, J. H. Molden: a Pre- and Post-processing Program for Molecular and Electronic Structures. *J. Comput.-Aided Mol. Des.* **2000**, *14*, 123–134.
- (40) Womack, C. C.; Fang, W.-H.; Straus, D. B.; Butler, L. J. Assessing an Impulsive Model for Rotational Energy Partitioning to Acetyl Radicals from the Photodissociation of Acetyl Chloride at 235 nm. *J. Phys. Chem. A* **2010**, *114*, 13005–13010.
- (41) McKown, B. G.; Ceriotti, M.; Womack, C. C.; Kamarchik, E.; Butler, L. J.; Bowman, J. M. Effects of High Angular Momentum on the Unimolecular Dissociation of  $\text{CD}_2\text{CD}_2\text{OH}$ . *J. Phys. Chem. A* **2013**, *117*, 10951–10963.
- (42) Brynteson, M. D.; Butler, L. J. Predicting the Effect of Angular Momentum on the Dissociation Dynamics of Highly Rotationally Excited Radical Intermediates. *J. Chem. Phys.* **2015**, *142*, 054301.
- (43) Ruscic, B., Active Thermochemical Tables (ATcT) values based on ver. 1.112 of the Thermochemical Network, 2013; available at [ATcT.anl.gov](http://ATcT.anl.gov).
- (44) Bozkaya, U.; Turney, J. M.; Yamaguchi, Y.; Schaefer, H. F., III. The Lowest-lying Electronic Singlet and Triplet Potential Energy Surfaces for the HNO-NOH System: Energetics, Unimolecular Rate Constants, Tunneling and Kinetic Isotope Effects for the Isomerization and Dissociation Reactions. *J. Chem. Phys.* **2012**, *136*, 164303.
- (45) Niu, B.; Shirley, D. A.; Bai, Y. High Resolution Photoelectron Spectroscopy and Femtosecond Intramolecular Dynamics of  $\text{H}_2\text{CO}^+$  and  $\text{D}_2\text{CO}^+$ . *J. Chem. Phys.* **1993**, *98*, 4377–4390.
- (46) Dodson, L. G.; Shen, L.; Savee, J. D.; Eddingsas, N. C.; Welz, O.; Taatjes, C. A.; Osborn, D. L.; Sander, S. P.; Okumura, M. VUV Photoionization Cross Sections of  $\text{HO}_2$ ,  $\text{H}_2\text{O}_2$ , and  $\text{H}_2\text{CO}$ . *J. Phys. Chem. A* **2015**, *119*, 1279–1291.
- (47) Huber, K. P.; Herzberg, G. *Molecular Spectra and Molecular Structure, IV. Constants of Diatomic Molecules*; Van Nostrand Reinhold Company, 1979.
- (48) Booth, R. S.; Brynteson, M. D.; Lee, S.-H.; Lin, J. J.; Butler, L. J. Further Studies into the Photodissociation Pathways of 2-Bromo-2-nitropropane and the Dissociation Channels of the 2-Nitro-2-propyl Radical Intermediate. *J. Phys. Chem. A* **2014**, *118*, 4707–4722.
- (49) Butler, L. J.; Krajnovich, D.; Lee, Y. T.; Ondrey, G. S.; Bersohn, R. The Photodissociation of Nitromethane at 193 nm. *J. Chem. Phys.* **1983**, *79*, 1708–1722.
- (50) Miller, J. L.; McCunn, L. R.; Krisch, M. J.; Butler, L. J.; Shu, J. Dissociation of the Ground State Vinyloxy Radical and its Photolytic Precursor Chloroacetaldehyde: Electronic Nonadiabaticity and the Suppression of the H+ketene Channel. *J. Chem. Phys.* **2004**, *121*, 1830–1838.
- (51) Nelson, L.; Shanahan, I.; Sidebottom, H. W. Kinetics and Mechanism for the Oxidation of 1,1,1-Trichloroethane. *Int. J. Chem. Kinet.* **1990**, *22*, 577–590.
- (52) Watanabe, K.; Matsunaga, F. M.; Sakai, H. Absorption Coefficient and Photoionization Yield of NO in the Region 580–1350 Å. *Appl. Opt.* **1967**, *6*, 391–396.

- (53) Watanabe, K.; Matsunaga, F. M.; Sakai, H. Erratum to ref 52. *Appl. Opt.* **1967**, *6*, 1220.
- (54) Dribinski, V.; Potter, A. B.; Demyanenko, A. V.; Reisler, H. Photodissociation Dynamics of the CH<sub>2</sub>Cl Radical: Ion Imaging Studies of the Cl+CH<sub>2</sub> Channel. *J. Chem. Phys.* **2001**, *115*, 7474–7484.
- (55) Potter, A. B.; Dribinski, V.; Demyanenko, A. V.; Reisler, H. Competitive Channels in the Jet-cooled Photodissociation of the CH<sub>2</sub>Cl Radical. *Chem. Phys. Lett.* **2001**, *349*, 257–265.
- (56) Levchenko, S. V.; Demyanenko, A. V.; Dribinski, V. L.; Potter, A. B.; Reisler, H.; Krylov, A. I. Rydberg-valence Interactions in CH<sub>2</sub>Cl→CH<sub>2</sub>+Cl Photodissociation: Dependence of Absorption Probability on Ground State Vibrational Excitation. *J. Chem. Phys.* **2003**, *118*, 9233–9240.
- (57) Townsend, D.; Lee, S. K.; Suits, A. G. DC Slice Imaging of CH<sub>3</sub>Cl Photolysis at 193.4 nm. *J. Phys. Chem. A* **2004**, *108*, 8106–8114.
- (58) Wang, F.; Lipciuc, M. L.; Kartakoullis, A.; Glodic, P.; Samartzis, P. C.; Yang, X.; Kitsopoulos, T. N. Slice Imaging of Methyl Bromide Photofragmentation at 193 nm. *Phys. Chem. Chem. Phys.* **2014**, *16*, 599–606.
- (59) Zhu, R. S.; Lin, M. C. CH<sub>3</sub>NO<sub>2</sub> decomposition/isomerization mechanism and product branching ratios: An *ab initio* chemical kinetic study. *Chem. Phys. Lett.* **2009**, *478*, 11–16.
- (60) Isegawa, M.; Liu, F.; Maeda, S.; Morokuma, K. *Ab initio* reaction pathways for photodissociation and isomerization of nitromethane on four singlet potential energy surfaces with three roaming paths. *J. Chem. Phys.* **2014**, *140*, 244310.
- (61) Ess, D. H.; Wheeler, S. E.; Iafe, R. G.; Xu, L.; Çelebi-Ölçüm, N.; Houk, K. N. Bifurcations on Potential Energy Surfaces of Organic Reactions. *Angew. Chem., Int. Ed.* **2008**, *47*, 7592–7601.
- (62) Ammal, S. C.; Yamataka, H.; Aida, M.; Dupuis, M. Dynamics-Driven Reaction Pathway in an Intramolecular Rearrangement. *Science* **2003**, *299*, 1555–1557.
- (63) Lourderaj, U.; Park, K.; Hase, W. L. Classical Trajectory Simulations of Post-transition State Dynamics. *Int. Rev. Phys. Chem.* **2008**, *27*, 361–403.
- (64) López, J. G.; Vayner, G.; Lourderaj, U.; Addepalli, S. V.; Kato, S.; deJong, W. A.; Windus, T. L.; Hase, W. L. A Direct Dynamics Trajectory Study of F<sup>-</sup> + CH<sub>3</sub>OOH Reactive Collisions Reveals a Major Non-IRC Reaction Path. *J. Am. Chem. Soc.* **2007**, *129*, 9976–9985.